KLEIN TUNNELING IN α-(BEDT-TTF)$_2$I$_3$ ORGANIC COMPOUND

by

Ümmü Seleme Nizam

B.S., Mathematics, Boğaziçi University, 2014

Submitted to the Institute for Graduate Studies in
Science and Engineering in partial fulfillment of
the requirements for the degree of
Master of Science

Graduate Program in Physics
Boğaziçi University
2019

ACKNOWLEDGEMENTS

I would like to thank my co-advisor Prof. Metin Arık and Dr. Can Yeşilyurt for their continous assist, guidance, and helpfull discussions.

I am grateful to my family for encouraging me throughout my thesis study.

Last but not the least I am really thankful to my friends Berare Göktürk, Şelale Şahin, and İrem Mantar for their valuable friendship and support.

ABSTRACT

KLEIN TUNNELING IN α-(BEDT-TTF)$_2$I$_3$ ORGANIC COMPOUND

The term Klein tunnelling refers to the counterintuitive phenomenon in which an incoming particle can perfectly transmit through a potential barrier even when the barrier height exceeds the particle's rest energy. This phenomenon has been made accessible by the properties of graphene and 3D Weyl semimetals. Recently, it has been demonstrated that the quasi-2D organic conductor α-(BEDT-TTF)$_2$I$_3$ exhibits a zero-gap state under uniaxial pressure along the stacking axis of BEDT-TTF molecules. It has been shown that the low-energy quasiparticles in this organic compound are massless Dirac fermions, i.e. its charge carriers obey the Weyl equation. In this Master's thesis we investigate the tunnelling effect in α-(BEDT-TTF)$_2$I$_3$ under the presence of hypothetical square electric potential and magnetic field. We show that although the application of electric potential does not cause asymmetric transmission profiles in 3D Weyl semimetals, the presence of tilt parameter in the energy dispersion relation renders the transmission profile asymmetric in the presence of a square potential barrier with constant height. Allowed transmission angle range increases with increasing potential barrier height. Besides, we demonstrate that the perfect transmission angles which allow the barrier to be nearly transparent are shifted by application of magnetic field on the central region.

ÖZET

α-(BEDT-TTF)$_2$I$_3$ ORGANİK BİLEŞİĞİNDE KLEİN TÜNELLEMESİ

Klein tünellemesi, potansiyel bariyere gelen elektronların, enerjileri bariyerden daha düşük olduğunda bile, potansiyel bariyer içinde ilerlemeye devam etmesi olayına verilen addır. Bu olay, grafen ve 3 boyutlu Weyl yarı metallerin özellikleriyle beraber erişilebilir kılınmaktadır. Yakın geçmişte, iki boyutlumsu organik iletken α-(BEDT-TTF)$_2$I$_3$'ün, BEDT-TTF moleküllerinin yığılma ekseni boyunca basınç uygulanması halinde, yasak enerji aralığının sıfır olduğu kanıtlanmıştır. Bu organik materyaldeki düşük enerjili kuazi-parçacıkların kütlesiz Dirac parçacıklara benzediği gösterilmiştir, yani bu materyaldeki yük taşıyıcılar Weyl denklemi ile betimlenmektedir. Bu yüksek lisans tezinde α-(BEDT-TTF)$_2$I$_3$ materyalinde, farazi bir potansiyel bariyer ve manyetik alan varlığında tünelleme etkisini inceledik. Elektriksel potansiyel asimetrik iletim profiline neden olmadığı halde, enerji özdeğerindeki eğiklik parametresi, sabit yüksekliğe sahip potansiyel bariyer altında iletim profilini asimetrik hale getirmektedir. Potansiyel bariyer yüksekliğinin artmasıyla beraber izin verilen iletim açılarının menzili de artmaktadır. Bunun yanı sıra, bariyeri neredeyse şeffaflaştıran iletim açılarının, manyetik alan etkisi altında değiştiğini gösterilmiştir.

TABLE OF CONTENTS

LIST OF FIGURES

LIST OF TABLES

LIST OF SYMBOLS

l_B	Magnetic Length
γ_μ	Gamma Matrices
$\delta_{\mu\nu}$	Euclidean Metric
σ_μ	Pauli Spin Matrices
γ^μ	Contravariant Gamma Matrices
$\eta^{\mu\nu}$	Minkowski Metric

LIST OF ACRONYMS/ABBREVIATIONS

2D	Two Dimensional
3D	Three Dimensional
QED	Quantum Electrodynamics
BZ	Brillouin Zone
nn	Nearest-Neighbour
nnn	Next-Nearest-Neighbour
ET	BEDT-TTF (bis(ethylenedithiolo)tetrathiofulvalene)
DF	Dirac Fermion
WP	Weyl Point
WS	Weyl Semimetal
WF	Weyl Fermion
TB	Tight-Binding

1. INTRODUCTION

In recent years, Dirac and Weyl semimetals (WSs) have attracted considerable attention in the scientific world [10–13]. There is a good deal of reasons that these materials have been brought to the forefront of modern condensed matter research. Their defining feature is that they have band structure with band crossing points in the vicinity of which the energy dispersion relation $\mathcal{E}(\mathbf{k})$ is linear. The effective Hamiltonian describing Weyl fermions in the bulk of 3D WSs has been, theoretically, demonstatrated to be robust against perturbation since the Hamiltonian contains three Pauli matrices [14]. The low-enegry quasiparticles in these semimetals behave as massless relativistic particles where the Fermi velocity $v_F \approx 10^6$ ms^{-1} plays the role of the speed of light. It has been demonstrated that Weyl nodes in the bulk of the material can be interpreted as magnetic monopoles in momentum space and they must occur in pairs of opposite chirality due to the fermion doubling theorem of Nielsen and Ninomiya [15, 16]. Owing to the chiral nature of their massless fermions, tunnelling through a potential barrier in these materials is different from the case of massive electrons. The former can penetrate through a high potential barrier unlike the case of the conventional tunnelling in which the transmission probability decays exponentially with increasing potential height. This absence of normal backscattering was originally introduced by O. Klein [17]. However, in his original work he examined the reflection of massive, non-relativistic, particles at a potential jump and he concluded that the barrier becomes nearly transparent solely if the potential exceeds electron's rest energy. Because of this condition, observation of Klein-like tunnelling was thought to be impossible. It has been shown that the exfoliation of graphene, which is a 2D Dirac semimetal, paves the way for Klein tunnelling to be tested experimentally [1]. This is because the transparency condition of the barrier has been eliminated using the fact that the effective mass of electrons on graphene is zero. Moreover, the existence of magic angles, at which perfect tunneling occurs, has been investigated in single-layer and bilayer graphene [18]. Casanova *et al.* have proposed the quantum simulation of $1 + 1$ Dirac equation with repulsive potential for positive energy particles [19].

They have discussed how electric potentials cause the perfect transmission through the barrier and showed, also, how to engineer scalar and pseudo-scalar potentials by manipulating two trapped ions. Furthermore, Salger *et al.* have observed the analog of Klein tunneling by means of an experiment which is based on the ultracold rubidium atoms in a Fourier-synthesized lattice potential [20]. Their experiment simulates the conversion of a particle into its antiparticle during the transmission of the potential barrier. On the other hand, the suppression of the transmission of normally incident electrons on single-layer graphene under the influence of magnetic field has been demonstrated [21]. Besides, Weyl semimetals [22–24] have been thought to be ideal candidates for tunnelling applications because of the chiral nature of their quasiparticles [2]. Klein tunnelling has also been investigated in these materials under the magnetic field effect [2, 25] and Yeşilyurt *et al.* have revealed the perfect transmission rings [2].

In this Master's thesis, we have analysed Klein-like tunnelling in the organic compound α-(BEDT-TTF)$_2$I$_3$ under the influence of hypothetical potential barrier, with or without magnetic field effect, by considering electron wave functions in three regions. Organic charge transfer salt (BEDT-TTF)$_2$I$_3$ has attracted attention for three decades. Among the five structural phases, α-phase has drawn more attention due to the following reason. Recent studies show that α-(BEDT-TTF)$_2$I$_3$ exhibits a zero-gap state with a tilted Dirac-cone-like dispersion near the band-crossing points under uniaxial pressure along the stacking axis of the BEDT-TTF molecules. BEDT-TTF molecule is also called ET. It has been shown that the low-energy quasiparticles in this organic compound are type-I Weyl fermion. α-(BEDT-TTF)$_2$I$_3$ exhibits many exotic properties because of which it is thought to provide a ground for a new type of Weyl fermions. It may be considered as a candidate material for tunnelling applications.

This thesis is organized as follows. Chapter 1 is devoted to the phenomenon of Klein tunnelling which is named after O. Klein. In the following chapter, chiral tunnelling in graphene and 3D Weyl semimetals are reviewed. In Chapter 3, we continue with lattice structure and electronic states under uniaxial pressure of α-(BEDT-TTF)$_2$I$_3$.

Afterwards, Klein tunnelling in this organic compound is examined. We calculated transmission probability through a 100-nm-wide potential barrier by means of matching of the wave functions for incident, propagated, and transmitted waves at the barrier interfaces. We, then, obtained the perfect transmission angles caused by the resonance of Fermi wave vector at the specific barrier length. Therefore, the angular dependence of transmission profile was analyzed in the case of different applied potential V_0 and under the influence of magnetic field. This is followed by the conclusion in Chapter 4.

1.1. The Klein Paradox

Consider a free particle with spin-$\frac{1}{2}$ and energy $\mathcal{E}$ satisfying the relation $\mathcal{E}^2 = p^2c^2 + m^2c^4$, due to Einstein, where c stands for the speed of light, m for the rest mass of the particle and p is the momentum. This massive particle is described by the celebrated Dirac equation

$$(\gamma_\mu \partial_\mu + \frac{mc}{\hbar})\psi(x_0, \mathbf{r}) = 0 \tag{1.1}$$

where $\psi(x_0, \mathbf{r})$ represents the wave function of the particle, γ_μ with $\mu = 0, 1, 2, 3$ are 4×4 matrices given, in Sakurai's notation, by

$$\gamma_k = \begin{pmatrix} 0 & -i\sigma_k \\ i\sigma_k & 0 \end{pmatrix}, \quad \gamma_0 = \begin{pmatrix} \sigma_0 & 0 \\ 0 & -\sigma_0 \end{pmatrix}, \quad k = 1, 2, 3 \tag{1.2}$$

∂_μ is the 4-gradient and $\partial_0 := \frac{1}{i}\frac{\partial}{\partial x_0}$ [26]. σ_ks refer to the standard Pauli spin matrices for spin-$\frac{1}{2}$ particles, namely

$$\sigma_1 = \begin{pmatrix} 0 & 1 \\ 1 & 0 \end{pmatrix}, \sigma_2 = \begin{pmatrix} 0 & -i \\ i & 0 \end{pmatrix}, \sigma_3 = \begin{pmatrix} 1 & 0 \\ 0 & -1 \end{pmatrix}$$

and σ_0 is the 2×2 identity matrix. The 4×4 matrices γ_μ are called Dirac, or Gamma, matrices. This system can be concisely expressed using the anticommutation relation as $\{\gamma_\mu, \gamma_\nu\} = \gamma_\mu\gamma_\nu + \gamma_\nu\gamma_\mu = 2\delta_{\mu\nu}, \quad \mu\nu = 0, 1, 2, 3.$

Gamma matrices in this notation also satisfy the hermiticity condition, i.e. $\gamma_\mu^\dagger = \gamma_\mu$ and they are traceless. As additional information, one can express the Gamma matrices in Dirac representation or Weyl, chiral, representation. If we multiply Dirac equation (1.1) by γ_0 from the right, we obtain an equation in the Hamiltonian form $\mathcal{H}\psi = i\hbar\partial_t\psi$ where

$$\mathcal{H} = -i\hbar c\boldsymbol{\alpha}\cdot\nabla + mc^2\beta \tag{1.3}$$

with $\boldsymbol{\alpha} = \begin{pmatrix} 0 & \boldsymbol{\sigma} \\ \boldsymbol{\sigma} & 0 \end{pmatrix}$ and $\beta = \gamma_0$. The matrices α_k $(k = 1,2,3)$ and β satisfy the following relations

$$\{\alpha_k, \beta\} = 0, \quad \beta^2 = 1, \quad \text{and} \quad \{\alpha_i, \alpha_j\} = 2\delta_{ij}.$$

To understand the essence of Klein tunnelling we place dealing with Dirac equation in three dimension on one side and continue with one dimensional equation. Hence, it is no more necessary to use the four-component Dirac spinor. The choice of $\gamma_0 = \sigma_z$ and $\gamma_1 = \sigma_x$ complies with the requirement $\gamma_i\gamma_j + \gamma_j\gamma_i = 2\delta_{ij}$. Through this choice of γ matrices, one dimensional Dirac equation (1.1) takes the form

$$(c\hbar\sigma_x\partial_x + mc^2 - i\hbar\sigma_z\partial_t)\psi(x, ct) = 0. \tag{1.4}$$

Therefore the Dirac Hamiltonian in one dimension can be obtained by multiplying the above equation σ_z from the right

$$\mathcal{H} = -c\sigma_y p_x + mc^2\sigma_z. \tag{1.5}$$

The plane wave solution to the above equation can be written as

$$\psi(x,t) = \begin{pmatrix} 1 \\ -\frac{i\hbar ck}{\mathcal{E}+mc^2} \end{pmatrix} e^{ikx} e^{-\frac{i\mathcal{E}t}{\hbar}} \tag{1.6}$$

where $k^2 \equiv \frac{(\mathcal{E}-mc^2)(\mathcal{E}+mc^2)}{c^2\hbar^2}$.

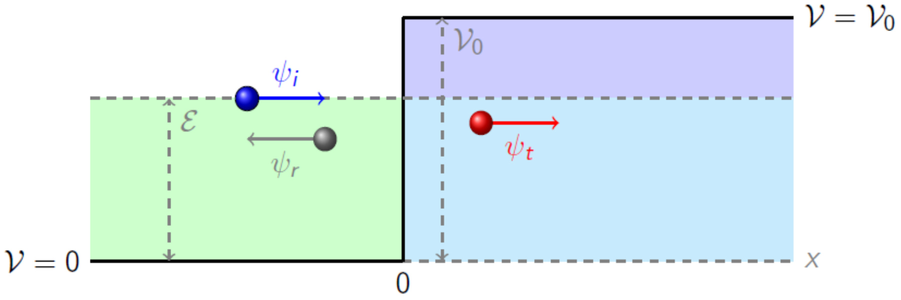

Figure 1.1. Klein step.

In the presence of the Klein step, i.e. $V(x) = V_0, x > 0; \quad V(x) = 0$, otherwise, the effective Hamiltonian (1.5) reads

$$\mathcal{H} = -c\sigma_y p_x + mc^2\sigma_z + V(x)$$

and Dirac equation (1.4), then, becomes

$$(c\hbar\sigma_x\partial_x + mc^2 - (\mathcal{E} - V(x))\sigma_z)\psi(x) = 0. \tag{1.7}$$

Assume that a particle with energy $\mathcal{E}$ approaches the vertical step potential from the left as shown in Figure 1.1. Therefore, solution of Equation 1.7 for the region to the left of the Klein step can be written as a superposition of incident and reflected waves and is given as follows:

$$\psi_l(x) = \begin{pmatrix} \psi_1(x) \\ \psi_2(x) \end{pmatrix} = \begin{pmatrix} 1 \\ -\frac{i\hbar ck}{\mathcal{E}+mc^2} \end{pmatrix} e^{ikx} + r \begin{pmatrix} 1 \\ \frac{i\hbar ck}{\mathcal{E}+mc^2} \end{pmatrix} e^{-ikx}. \tag{1.8}$$

In the region where the potential V_0 is applied we consider two distinct cases:

(i) $\mathcal{E} - mc^2 < V_0 < \mathcal{E} + mc^2$ or $V_0 - mc^2 < \mathcal{E} < V_0 + mc^2$

(ii) $|V_0| > \mathcal{E} + mc^2$.

Suppose V_0 satisfies the first case. Then, transmitted portion of the wave function can be expressed as

$$\psi_r(x) = t \begin{pmatrix} 1 \\ \frac{c\hbar\kappa}{mc^2+(\mathcal{E}-V_0)} \end{pmatrix} e^{-\kappa x} \tag{1.9}$$

where κ is defined by $\kappa^2 \equiv \frac{(mc^2-(\mathcal{E}-V_0))(mc^2+(\mathcal{E}-V_0))}{c^2\hbar^2}$. Note that $e^{\kappa x}$ exponentially increases with x and is not an element of physical Hilbert space. Applying the boundary conditions at the barrier interface $x = 0$ we reach the conclusion that the reflection probability $R = |r|^2 = |\frac{\kappa+ik}{\kappa-ik}|^2$ is unity. This means that incoming electrons can not penetrate into the classically forbidden region under the case of a potential which does not exceed the sum of the electron's total and rest energy, $\mathcal{E} + mc^2$.

For larger V_0, i.e. $\mathcal{E} + mc^2 < V_0$, the top and bottom components of the wave function ψ for incident and transmitted region are as follows:

$$\begin{aligned} \psi_1(x) &= \begin{cases} e^{ikx} + re^{-ikx}, & \text{if } x < 0 \\ te^{iqx}, & \text{if } x > 0 \end{cases} \\ \psi_2(x) &= \begin{cases} -\frac{c\hbar ik}{\mathcal{E}+mc^2}e^{ikx} + r\frac{c\hbar ik}{\mathcal{E}+mc^2}e^{-ikx}, & \text{if } x < 0 \\ t\frac{c\hbar iq}{V_0-\mathcal{E}-mc^2}e^{iqx}, & \text{otherwise} \end{cases} \end{aligned} \tag{1.10}$$

where q denotes the wave vector within the barrier and is given by $q = -\frac{\sqrt{(V_0-\mathcal{E})^2-m^2c^4}}{c\hbar}$. The particle coming from the left will partly penetrate the barrier and the group velocity for transmitted portion must be positive, i.e. $\nu_g = \frac{\tilde{p}c^2}{\mathcal{E}-V_0} > 0$ where particle momentum $\tilde{p}$ satisfies $\tilde{p}^2c^2 = (V_0 - \mathcal{E})^2 - m^2c^4$ for $x > 0$. Since we assumed V_0 is much larger than total energy $\mathcal{E}$, the wave vector q has to be assigned its negative value.

Continuity of the wave function at $x = 0$ yields the following relations:

$$\begin{aligned} 1 + r &= t \\ \frac{-c\hbar i k}{\mathcal{E} + mc^2}(1 - r) &= \frac{c\hbar i q}{V_0 - \mathcal{E} - mc^2} t. \end{aligned} \tag{1.11}$$

Substituting $t = 1 + r$ into the second one we obtain the following equality:

$$\frac{1 - r}{1 + r} = \frac{-q}{k} \frac{(\mathcal{E} + mc^2)}{(V_0 - \mathcal{E} - mc^2)} \tag{1.12}$$

Let γ be defined by $\gamma \equiv \frac{-q}{k} \frac{(\mathcal{E}+mc^2)}{(V_0-\mathcal{E}-mc^2)}$ (or equivalently, $\gamma = \sqrt{\frac{V_0-\mathcal{E}+mc^2}{V_0-\mathcal{E}-mc^2}} \sqrt{\frac{\mathcal{E}+mc^2}{\mathcal{E}-mc^2}}$). Then, this gives the expression for reflection and transmission probabilities

$$R = \left| \frac{1 - \gamma}{1 + \gamma} \right|^2 \quad \text{and} \quad T = \frac{4\gamma}{|1 + \gamma|^2} \tag{1.13}$$

where the latter follows from $R + T = 1$. This result seems not paradoxical. If, however, we consider the case V_0 approaches infinity, we encounter a surprising situation, namely a non-zero transmission probability since γ has a finite limit at infinity. This means that incident fermions can penetrate into the classically forbidden region regardless of the potential height V_0. This exotic phenomenon is called Klein paradox after being described by O. Klein, in 1929 [17]. To observe experimentally the Klein-like tunnelling of massive particles, applied potential must exceeds at least twice the particle rest energy $2m_ec^2$, i.e. $V_0 > 1$ MeV. Considering the energy dispersion relation $\mathcal{E}(k)$ there is a gap between conduction (upper) and the valence (lower) bands as shown in Figures 1.2 and 1.3. Any step height which satisfies the requirement $V_0 > 2m_ec^2$, makes the matching between electronic states outside the step and hole states inside possible. This matching may give cause for the penetration of incident electrons through a high potential step. In other words, the probability of tunnelling increases as the applied potential is increased.

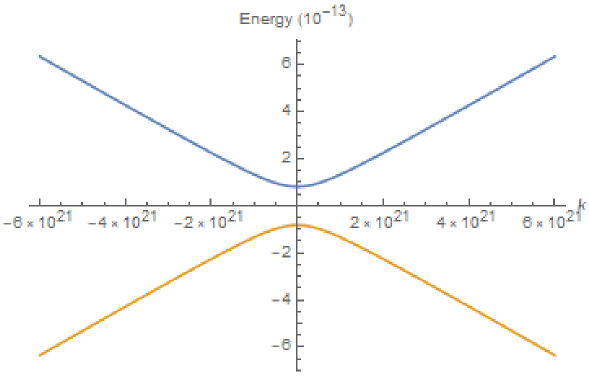

Figure 1.2. Band gap. For massive fermions case, the conduction (upper) and the valence (lower) bands are separated by a band gap, $\mathcal{E}_g = 2m_ec^2$.

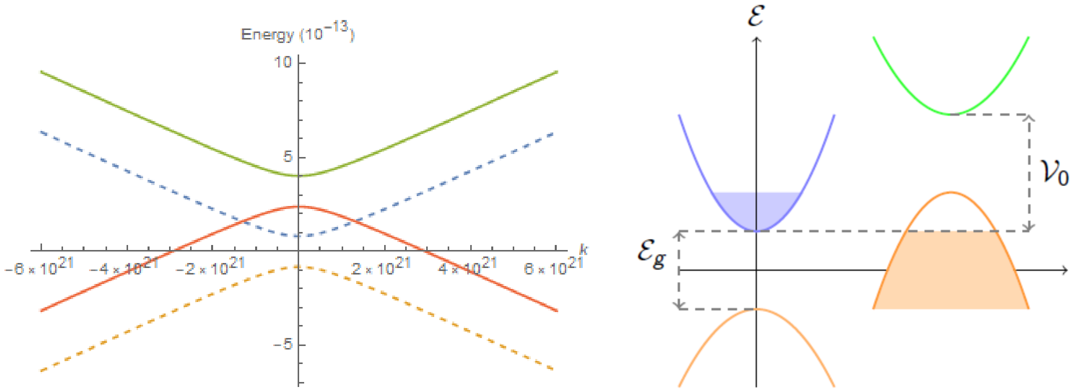

Figure 1.3. Matching the electronic states outside the Klein step with the hole state inside. In each plot, blue (dashed) and yellow (dashed) bands are obtained outside the step as green (straight) and orange (straight) ones represent the energy dispersion inside the step. For the left plot step height V_0 is chosen to be $V_0 = 2$ MeV.

In order to analyse this absence of backscattering of fermions in a more physical ground, we consider a square potential barrier with height $V(x)$ which is defined as

$$V(x) = V_0, |x| < a; \quad V(x) = 0, |x| > a.$$

Incident fermions would be expected not to be able to distinguish between a wide barrier and a Klein step [27].

Following the same procedure, with the condition $V_0 > \mathcal{E} + mc^2$, one can get the wave functions for incident, reflected, and transmitted region

$$\begin{aligned} \psi_1(x) &= \begin{cases} e^{ikx} + re^{-ikx}, & x < -a \\ \tilde{a}e^{i\kappa x} + \tilde{b}e^{-i\kappa x}, & -a < x < a \\ te^{ikx}, & x > a \end{cases} \\ \psi_2(x) &= \begin{cases} -i\alpha(e^{ikx} - re^{-ikx}), & x < -a \\ i\beta(\tilde{a}e^{i\kappa x} - \tilde{b}e^{-i\kappa x}), & -a < x < a \\ -i\alpha te^{ikx}, & x > a \end{cases} \end{aligned} \tag{1.14}$$

where $\alpha = \frac{\sqrt{\mathcal{E}-mc^2}}{\sqrt{\mathcal{E}+mc^2}}$, $\beta = \frac{\sqrt{V_0-\mathcal{E}-mc^2}}{\sqrt{V_0-\mathcal{E}+mc^2}}$, and we have assumed the particle approaches the barrier from the left. The wave vectors k and κ are as described in Equations 1.6 and 1.9.

Applying the boundary conditions at the barrier interfaces $x = -a$ and $x = a$ one can get the expressions for reflection and transmission amplitudes

$$\begin{aligned} r &= \frac{e^{-2iak}(-1e^{4ia\kappa})(\alpha^2\beta^2 - 1)}{-1 + e^{4ia\kappa} + 2\alpha\beta + 2e^{4ia\kappa}\alpha\beta - \alpha^2\beta^2 + e^{4ia\kappa}\alpha^2\beta^2} \\ t &= \frac{4e^{-2ia(k-\kappa)}\alpha\beta}{-1 + e^{4ia\kappa} + 2\alpha\beta + 2e^{4ia\kappa}\alpha\beta - \alpha^2\beta^2 + e^{4ia\kappa}\alpha^2\beta^2} \end{aligned} \tag{1.15}$$

respectively. These amplitudes lead to reflection and transmission probabilities

$$R = |r|^2 = \frac{(1-\alpha^2\beta^2)^2 \sin^2(2a\kappa)}{4\alpha^2\beta^2 + (1-\alpha^2\beta^2)^2 \sin^2(2a\kappa)} \tag{1.16}$$

$$T = |t|^2 = \frac{4\alpha^2\beta^2}{4\alpha^2\beta^2 + (1-\alpha^2\beta^2)^2 \sin^2(2a\kappa)}. \tag{1.17}$$

Transmission resonance occurs when $\kappa = n\pi/2a$, where $n \in \mathbb{Z}$, which corresponds to energy levels $\mathcal{E}_n = V_0 - \sqrt{(mc^2)^2 + (\frac{n\pi}{2a})^2 c^2 \hbar^2}$. The particle having energy $\mathcal{E}_n$, therefore, can pass through the barrier without any reflection.

As a becomes very large for fixed m, $\mathcal{E}$ and V_0, $\sin(2a\kappa)$ oscillates very rapidly so that one can average over the phase angle $2a\kappa$ to find the limit [27]

$$R_\infty = \frac{(1-\alpha^2\beta^2)^2}{8\alpha^2\beta^2 + (1-\alpha^2\beta^2)^2}, \quad T_\infty = \frac{8\alpha^2\beta^2}{8\alpha^2\beta^2 + (1-\alpha^2\beta^2)^2}. \tag{1.18}$$

The above results are not identical with the probabilities (1.13) in the case of Klein step, however, they show the same characteristics. Hence, the square potential barrier demonstrates Klein tunnelling as well. Besides, this phenomenon was also investigated by Sauter [28] and Hund [29]. While Sauter discussed the scattering off a potential representing constant electric field in the context of Dirac equation, Hund contributed to the subject by looking at a potential barrier from the aspect of quantum field theory [27].

2. KLEIN TUNNELLING IN GRAPHENE AND WEYL SEMIMETALS

2.1. Graphene

Graphene is a 2D semiconductor with a linear energy spectrum. Its low energy quasiparticles are described by the 2D Dirac Hamiltonian

$$\mathcal{H} = -i\hbar v_F \boldsymbol{\sigma} \cdot \boldsymbol{\nabla} \tag{2.1}$$

rather than the Schrödinger equation, where v_F is the Fermi velocity being approximately 300 times smaller than the speed of light c and $\boldsymbol{\sigma} = (\sigma_x, \sigma_y)$ are standard Pauli matrices. The pseudo-spin σ represents the sublattice index, not the real electronic spin. This 2D Dirac Hamiltonian, correspondingly the linear energy dispersion, is an immediate consequence of graphene's honeycomb lattice structure. The electronic band structure of graphene is usually obtained by nearest-neighbor-tight-binding method. The energy dispersion relation results

$$\mathcal{E}_{\mathbf{k}}^{\xi} = \xi t \sqrt{1 + 4\cos(\sqrt{3}\frac{a_0 k_x}{2})\cos(3\frac{a_0 k_y}{2}) + 4\cos^2(\sqrt{3}\frac{a_0 k_x}{2})} \tag{2.2}$$

where $a_0 \approx 1.42$ Å, $t = -3$ eV and $\xi = \pm$ denotes conduction ($\xi = +$) and valence bands ($\xi = -$). The cosine-like energy bands coincide at two inequivalent points in the first Brillouin zone, namely $\mathbf{K}$ and $\mathbf{K}'$, and the Fermi level is placed at these points. These are called Dirac points. In the vicinity of the contact points, the Hamiltonian describing the low energy quasiparticles is found to be the 2D Dirac Hamiltonian (2.1) and the energy $\mathcal{E}$ of the particles varies linearly with momentum, i.e. $\mathcal{E} = \pm\hbar v_F |\mathbf{k}|$ where $v_F \approx 10^6$ ms^{-1}. The lattice structure of graphene and the physics of Dirac fermions on graphene have been reviewed in References [8, 30]. Also, one can find the detailed explanations in Appendix A.

By virtue of its linear spectrum, quasiparticles in graphene will act differently from those in semiconductors which have parabolic energy dispersion relation [1].

Graphene has aroused tremendous interest since its discovery in 2004 [31] due to three phenomena: its conductivity which never falls below the conductance quantum $G_0 = 2e^2/h$, half-integer quantum Hall effect, and cyclotron mass of massless fermions [32]. Another important reason for rising interest in graphene is that ballistic transport of fermions in graphene occurs up to 0.3 μm at 300 K which corresponds to thousands of interatomic distance [33]. Furthermore, it was reported in 2006 that chiral tunnelling of fermions in graphene can be observed experimentally [1]. It is the first material which can be regarded as a medium for elucidating Klein tunnelling. This has given rise to the understanding that graphene can be seen as a condensed-matter analogue of 2+1 dimensional QED and it provides an effective ground for relativistic quantum phenomena to be tested experimentally [33].

In the next subsection, chiral tunnelling in graphene is examined in detail.

2.1.1. Chiral Tunnelling and Klein Paradox in Graphene

As is stated, quasiparticles in graphene resemble massless Dirac fermions so that this system enables us to set up an experiment for realising Klein tunnelling. The general scheme is that we consider a rectangular shaped potential barrier, as shown in Figure 2.1, applied on a graphene sheet through y-axis such that

$$V(y) = \begin{cases} V_0 & \text{if } 0 < y < L \\ 0 & \text{otherwise} \end{cases} \tag{2.3}$$

where V_0 is constant and the incident electron is supposed to be coming from the left of the barrier at an angle ϕ with respect to x-axis. The potential acts identically on the sublattices A and B.

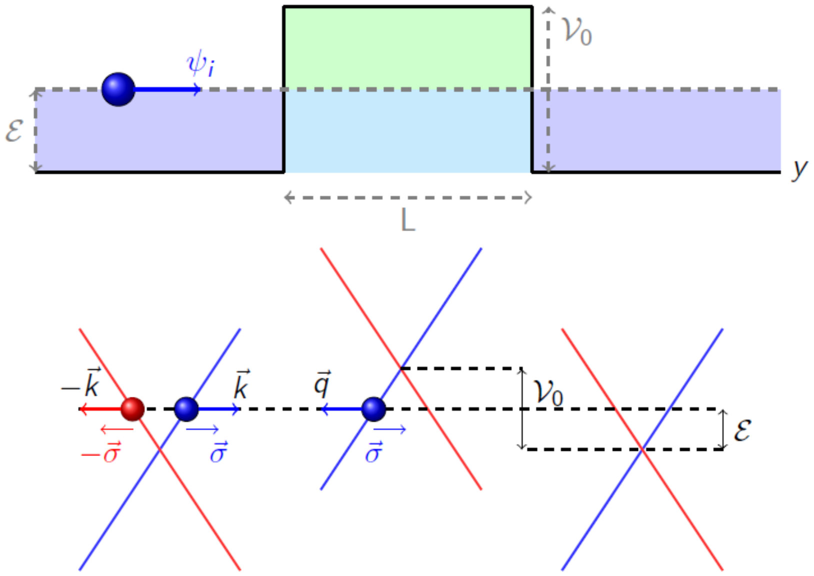

Figure 2.1. Tunnelling through a potential barrier in graphene. (Top) Potential barrier of height V_0 and width L. (Bottom) Schematic diagram of the spectrum of the low energy quasiparticles ob gaphene. The pseudospin $\boldsymbol{\sigma}$ is parallel(antiparallel) to the direction of motion of the electrons(holes). Figure from Reference [1].

It has been shown that such an electrostatic potential can be created by local chemical doping or electric field effect [1, 31, 32, 34]. A sufficiently strong potential which is repulsive for electrons leads to positron states inside the barrier [1]. AS we discussed in Chapter 1, absence of backscattering of electrons requires higher potential for massive particles. To observe experimentally the shift between electron-positron states of massive particles, the required energy must be larger than twice the particle rest energy $2m_ec^2$. In the case of massless fermions this requirement does not have to be satisfied. An electric field $E \approx 10^5$ V cm^{-1} is used in experiments to create such a potential and is sufficient to observe Klein tunnelling for quasiparticles in graphene [1].

Without loss of generality, we regard the effective Hamiltonian expanded around Dirac point $\mathbf{K}$

$$\mathcal{H} = \hbar v_F \begin{pmatrix} 0 & k_x - ik_y \\ k_x + ik_y & 0 \end{pmatrix}. \tag{2.4}$$

The 2D Dirac equation is, therefore, given by

$$\hbar v_F(\boldsymbol{\sigma}\cdot\mathbf{k})\psi_{\mathbf{k}} = \mathcal{E}_{\mathbf{k}}\psi_{\mathbf{k}} \tag{2.5}$$

where $\psi_{\mathbf{k}} \equiv (\psi_{1,\mathbf{k}}, \psi_{2,\mathbf{k}})$ is called a Dirac spinor. This two component wave function is the consequence of graphene's crystal symmetry. Here, $\boldsymbol{\sigma}$ is called pseudospin and denotes the sublattices A and B rather than the real spin of quasiparticles in graphene [1]. Since the transverse wave vector k_x is conserved throughout the motion, it is quite reasonable to make the ansatz

$$\psi_i(x,y) = e^{ik_x x}\phi_i(y), \quad i = 1,2.$$

The eigenstates of the Dirac Hamiltonian (2.4) is given by

$$\psi = \frac{1}{\sqrt{2}}\begin{pmatrix} 1 \\ \xi e^{i\phi} \end{pmatrix} \tag{2.6}$$

where we have defined $\phi \equiv \arctan(k_y/k_x)$ and $\xi = \pm$ denotes conduction (+) and valence (-) bands. With the help of the eigenstates corresponding to the eigenvalues $\mathcal{E}_\xi$ the top and bottom components of the wavefunction ψ for incident, reflected, and transmitted region may be found in the following form:

$$\psi_1(x,y) = \begin{cases} (e^{ik_y y} + re^{-ik_y y})e^{ik_x x}, & y < 0 \\ (ae^{iq_y y} + be^{-iq_y y})e^{ik_x x}, & 0 < y < L \\ te^{ik_y y}e^{ik_x x}, & y > L \end{cases} \tag{2.7}$$

$$\psi_2(x,y) = \begin{cases} s(e^{ik_y y}e^{i\phi} + re^{-ik_y y}e^{-i\phi})e^{ik_x x}, & y < 0 \\ s'(ae^{iq_y y}e^{i\theta} + be^{-iq_y y}e^{-i\theta})e^{ik_x x}, & 0 < y < L \\ ste^{i(k_y y+\phi)}e^{ik_x x}, & y > L \end{cases} \tag{2.8}$$

where the refraction angle has been defined by $\theta \equiv \arctan(\frac{q_y}{k_x})$, $s = \mathrm{sgn}[\mathcal{E}]$ and $s' = \mathrm{sgn}[\mathcal{E} - V_0]$.

Outside the barrier x and y-components of the wave vector $\mathbf{k}$ are $k_x = k_F \cos\phi$ and $k_y = k_F \sin\phi$, respectively, where $k_F = \frac{\mathcal{E}}{\hbar v_F}$. q_y denotes the y-component of the wave vector within the barrier and is given by $q_y = \sqrt{\frac{(\mathcal{E}-V_0)^2}{\hbar^2 v_F^2} - k_x^2}$. The boundary conditions are given by

$$
\begin{aligned}
&1 + r = a + b \\
&s(e^{i\phi} + re^{-i\phi}) = s'(ae^{i\theta} + be^{-i\theta}) \\
&ae^{iq_yL} + be^{-iq_yL} = te^{ik_yL} \\
&s'(ae^{iq_yL}e^{i\theta} + be^{-iq_yL}e^{-i\theta}) == ste^{ik_yL}e^{i\phi}.
\end{aligned}
\tag{2.9}
$$

Finally, with the help of the boundary conditions (2.9) arising from the continuity of the wave functions at the barrier interfaces, one can find the transmission coefficient t

$$
t = \frac{2ss' \sin\theta \sin\phi e^{-ik_yL}}{ss'(-e^{-iq_yL}\cos(\theta+\phi) + e^{iq_yL}\cos(\theta-\phi)) - 2i\sin(q_yL)}. \tag{2.10}
$$

The transmission probability $T = |t|^2$, therefore, can be calculated using the above equation,

$$
T = \frac{4\sin^2\theta\sin^2\phi}{1 + \cos(2\theta)\cos(2\phi) - (\cos 2\phi + \cos 2\theta)\cos(2q_yL) + 4\sin^2(q_yL)(1 - 2ss'\cos\theta\cos\phi)} \tag{2.11}
$$

and the ϕ-dependence of T under several conditions is shown in Figure 2.2.

Under the case of high potential $|V_0| \gg |\mathcal{E}|$ the transmission probability T can be reduced to

$$
T = \frac{\sin^2\phi}{1 - \cos^2\phi\cos^2(q_yL)}. \tag{2.12}
$$

It can be easily inferred from the last equation that under the resonance condition $q_y = \frac{n\pi}{L}, n = 0, \pm1, \pm2, \ldots$, the transmission probability becomes unity which indicates absence of backscattering of electrons in the presence of high potential.

It is more important to note that even in the case of a finite potential normally incident electrons can always penetrate the barrier as shown in Figure 2.2. This transparency is relevant to Klein tunnelling and it is the characteristic of massless Dirac and Weyl fermions [1]. As can be seen in Figure 2.3 for angles off normal, the transmission becomes height dependent. Analytically, one can find out the angles at which perfect tunnelling is realised by using resonance conditions

$$q_y = \sqrt{\frac{(\mathcal{E} - V_0)^2}{\hbar^2 v_F^2} - k_F^2 \cos^2 \phi} = \frac{n\pi}{L}, \quad n \in \mathbb{Z}. \tag{2.13}$$

This perfect tunnelling of fermions through high potential barriers is called paradox since it has never been directly observed [1]. Katsnelson *et al.* have shown that Klein tunnelling can be observed experimentally in graphene. One may interpret this transparency in terms of conservation of pseudospin $\boldsymbol{\sigma}$ [1]. An incoming fermion from the left can be transformed into the left-moving hole state or to the right-moving electron-state in the absence of pseudospin-flip process. As shown in Figure 2.1(bottom) charge carriers from the blue branch of the band diagram can be scattered to the states on the same branch and cannot be scattered into any states on the red branch. Therefore, matching the direction of pseudospin for quasiparticles across the barrier leads to perfect tunnelling.

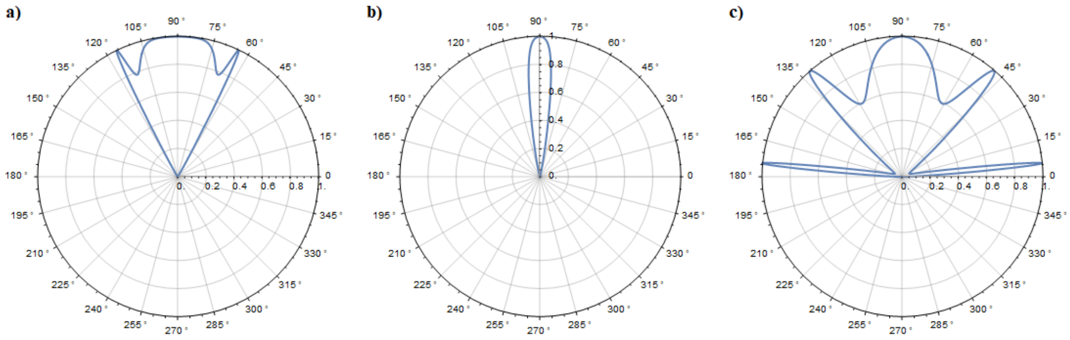

Figure 2.2. Transmission probability T through a 100-nm-wide barrier as a function of incident angle under the case of (a)$\mathcal{E}_F/2$, (b)63, and (c)200 meV potential barrier. The Fermi energy $\mathcal{E}_F$ is chosen to be approximately 83 meV. The figure is a reproduction of the result previously presented in Reference [1].

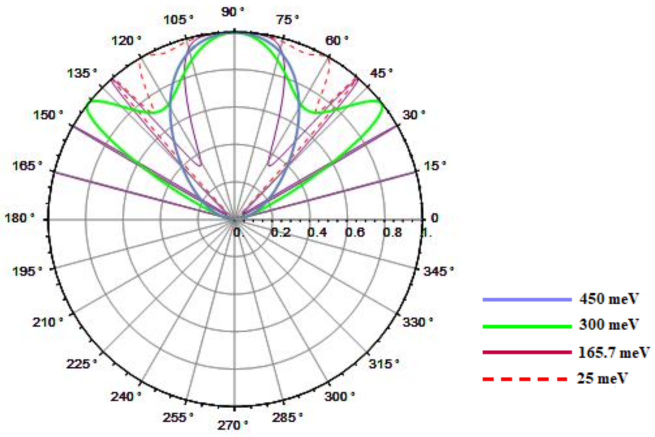

Figure 2.3. Angular dependence of the transmission probability in graphene systems. Transmission probability T through a 100-nm-wide barrier as a function of incident angle ϕ under the case of various potential V_0 and constant Fermi energy $\mathcal{E}_F = 82.9$ meV.

To make a comparison, we consider the effect of magnetic field on graphene for different electric potentials V_0. We assume a delta-function-like magnetic field is applied on graphene sheet perpendicularly, i.e. $B_z = B_0 l_B[\delta(y) - \delta(y-L)]$, causing a gauge potential $A_x = B_0 l_B[\Theta(y) - \Theta(y-L)]$ where $l_B = \sqrt{\frac{\hbar}{eB_0}}$ is the magnetic length. This magnetic barrier can be realized by a ferromagnetic stripe fabricated on top of the graphene sheet [35, 36]. The magnetic field gives rise to a change on the transverse wave vector along x-direction

$$k_x \longrightarrow \frac{\mathcal{E}_F \cos\theta + \mu v_F \sqrt{|B_0||e|\hbar}}{\hbar v_F}$$

and, thus, the wave vector inside the barrier along y-direction forms

$$q_y = \sqrt{\frac{(\mathcal{E}_F - V_0)^2}{\hbar^2 v_F^2} - (k_x + \mu\delta)^2}$$

where $\mu = \pm$ denotes the sign of the magnetic field and δ stands for the shift of the transverse wave vector. In this scenario, without loss of generality, the potential barrier is assumed to be placed on the y-axis, i.e. $V(y) = V_0, 0 < y < L; \quad V(y) = 0,$ otherwise.

Angular dependence of transmission probability in the case of constant magnetic barrier is shown in Figure 2.4. The pink plots in all three figures are obtained in the case of different potential barrier height without magnetic field effect. Fermi energy is chosen to be $\mathcal{E}_F = 83$ meV. Plots (a) and (b) are obtained at electrical potentials $V_0 = 63$ meV and $V_0 = 285$ meV, respectively while (c) is obtained in the case of $V_0 = 200$ meV. Blue and green plots, moreover, are acquired under the case of (a) $B_0 = 1.8\ T$, $B_0 = -1.8\ T$; (b) $B_0 = 1.5\ T$, $B_0 = -0.05\ T$; (c) $B_0 = 1.25\ T$, $B_0 = -1.25\ T$, respectively. Blue and green plots display the shift of the perfect transmission angles under different magnetic fields. This angle change corresponds to the sign alteration of the magnetic field $\mathbf{B}$. It can be seen from the leftmost figure that the perfect transmission angle is shifted in the presence of magnetic field effect. Furthermore, it is shown that the magnetic field effect renders the transmission profiles asymmetric with respect to normal incidence.

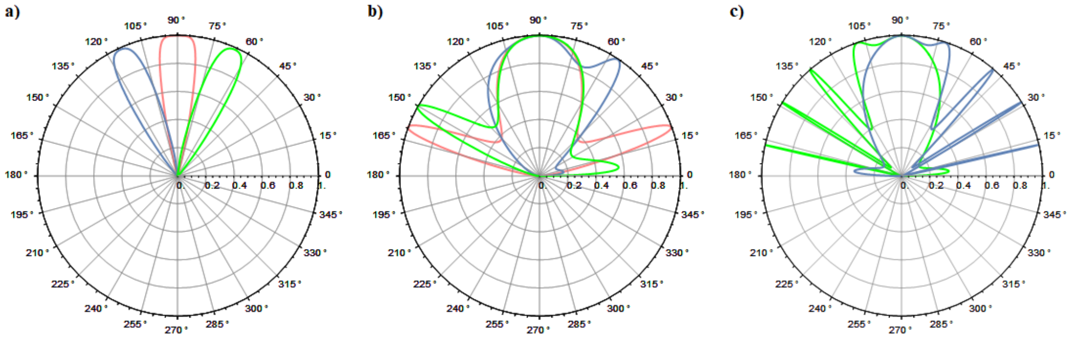

Figure 2.4. Angular dependence of transmission probability in graphene under the case of different configurations of the magnetic barrier for different electric potential V_0. The figure is a reproduction of the result previously presented in Reference [2].

2.2. Weyl Semimetals

A Weyl semimetal is a crystal whose low-energy excitations are massless fermions which are described by Weyl Hamiltonian

$$\mathcal{H}_{\pm} = \pm \hbar v_F (\sigma_x k_x + \sigma_y k_y + \sigma_z k_z) \tag{2.14}$$

where ± denotes chirality and k_i represents the crystal momentum. One may identify the chirality and helicity for the massless fermions. One can find the explanation in Appendix A. Weyl Hamiltonian is nothing but massless Dirac Hamiltonian (1.3) with the choice of γ^μ matrices (1.2). Massless Dirac equation may be written explicitly as

$$\hbar c \begin{pmatrix} 0 & \boldsymbol{\sigma}\cdot\mathbf{k} \\ -\boldsymbol{\sigma}\cdot\mathbf{k} & 0 \end{pmatrix} \begin{pmatrix} \psi_1 \\ \psi_2 \end{pmatrix} = i\hbar\gamma_0\partial_t \begin{pmatrix} \psi_1 \\ \psi_2 \end{pmatrix} \tag{2.15}$$

where ψ_is are two-component wave functions. If one take $\psi_1 = \phi_R + \phi_L$ and $\psi_2 = \phi_R - \phi_L$, the last equation for massless particles separates into two equations:

$$\begin{aligned} -i\hbar c\boldsymbol{\sigma}\cdot\nabla\phi_R &= i\hbar\partial_t\phi_R \\ i\hbar c\boldsymbol{\sigma}\cdot\nabla\phi_L &= i\hbar\partial_t\phi_L. \end{aligned} \tag{2.16}$$

The two component wave functions ϕ_R and ϕ_L describe a right-handed (spin parallel to the direction of motion) and the left-handed (spin antiparallel to the direction of motion) states of the massless fermions, respectively. This can be interpreted as decoupling a Dirac point into two points, which are called Weyl nodes, with opposite chirality as shown in Figure 2.5 and the details can be found in Appendix B.

Topological Weyl semimetals have recently aroused interest in condensed matter physics [10,11,14,24,37]. The characteristic feature of WSs is the appearance of linear band touching points at the Fermi energy. One cannot get rid of the Weyl point by small perturbations, e.g. altering the energy V_0 or Fermi velocity v_F. For instance, changing the Fermi velocity v_F can change the slope of the energy dispersion.

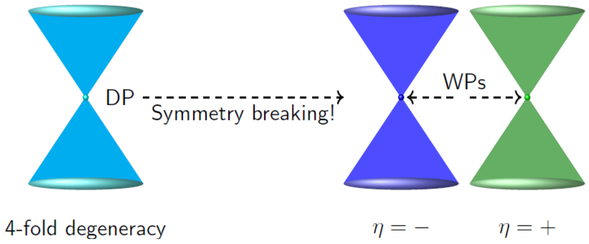

Figure 2.5. Splitting of a Dirac point. A four-fold degenerate Dirac point can be splitted into two Weyl points with opposite chirality by breaking time-reversal of inversion symmetry. $\eta = \pm$ denotes the chirality of the Weyl nodes.

The perturbation $\boldsymbol{\delta} \cdot \boldsymbol{\sigma}$ to the Weyl Hamiltonian (2.14) can only shift the touching point from zero to $\mathbf{k} = \mp\boldsymbol{\delta}/\hbar v_F$ in momentum space. This has something to do with the fact that the number of Pauli spin matrices and the momentum components are the same and the bands are non-degenerate with a given $\mathbf{k}$ [10]. To put the second condition more explicitly we consider the following argument: Assume that there exists time-reversal symmetry in the system which requires $\mathcal{E}_{n,\uparrow}(\mathbf{k}) = \mathcal{E}_{n,\downarrow}(-\mathbf{k})$. If a Weyl node occurs at some point $\mathbf{k_0}$ in BZ, then there must be another Weyl point $-\mathbf{k_0}$ with the same chirality. Due to the no-go theorem of Nielsen and Ninomiya [15, 16] the Weyl nodes must occur in pairs with opposite chirality. This is another important feature of massless Weyl fermions. Thus, there must be another Weyl point $\mathbf{k}_0^{'}$ with opposite chirality and accordingly $-\mathbf{k}_0^{'}$ because of time-reversal symmetry. If there is an inversion symmetry in the system which, in general, requires $\mathcal{E}_{n,\sigma}(\mathbf{k}) = \mathcal{E}_{n,\sigma}(-\mathbf{k})$, another Weyl point $-\mathbf{k_0}$ must occur with opposite chirality. In the presence of both time-reversal and inversion symmetry, the relation $\mathbf{k_0} = \mathbf{k}_0^{'}$ satisfies and each of two crossing points become 4-fold degenerate. This type of materials is called Dirac semimetals [12]. Consequently, either inversion or time-reversal symmetry exists in 3D Weyl semimetals in order for the Weyl nodes to be protected topologically.

Consider the most general Hamiltonian describing tilted WFs

$$\mathcal{H} = \hbar \sum_i (v_i \sigma_i + w_i) k_i \tag{2.17}$$

where w_i denotes the strength of the tilt of the energy dispersion along the ith direction. w_i is in the dimension of velocity. This Hamiltonian describes two types of tilted Weyl fermions: type-I and type-II, according to the value of tilt parameter ω, which is given as

$$\omega = \sqrt{\left(\frac{\omega_x}{v_x}\right)^2 + \left(\frac{\omega_y}{v_y}\right)^2}. \tag{2.18}$$

Without loss of generality we assume $v_i = v_F$ and $w_i = \tilde{v}$, constant along all direction. If $\tilde{v} < v_F$ then conduction and valence bands coincides at a single point and Weyl semimetals have a point-like Fermi surface at this node as shown in Figure 2.6. Weyl semimetal having this feature is classified as type-I Weyl semimetal. The first discovered type-I Weyl semimetal TaAs is reported theoreticaly by two groups in 2015 [23,37]. The experimental discovery was realized subsequently [22,37]. This family of materials includes TaP and NbAs [24, 38]. If $\tilde{v} > v_F$ the tilt parameter becomes larger than unity, i.e. $w > 1$. In this case the crossing point appears at the contact of electron and hole pockets as shown in Figure 2.6. Such Weyl semimetals are named type-II Weyl semimetals [3]. $\mathrm{WTe_2}$, $\mathrm{MoTe_2}$ and $\mathrm{W_xMo_{1-x}Te_2}$ are examples of type-II Weyl semimetals [3, 39–41].

2.2.1. Klein Tunnelling in Weyl Semimetals under the Influence of a Rectangular Potential Barrier and a Magnetic Field

After the introduction of Weyl semimetal we continue with examining chiral tunnelling phenomena in WSs. In the first instance, we scrutinise Klein tunnelling under the influence of a rectangular potential barrier. We assume that the potential is applied on the central region along the y-axis as shown in Figure 2.1. This potential barrier configuration may be obtained via alkaline metal doping or applying gate-voltage.

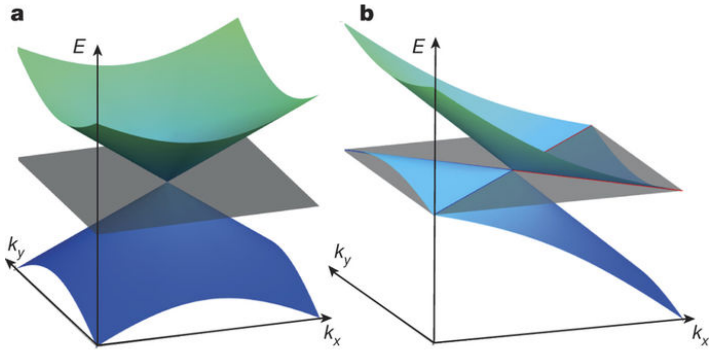

Figure 2.6. Type-I and type-II Weyl semimetals. (a) shows the energy dispersion of type-I Weyl semimetals. The grey plane indicates the Fermi level. In plot (b) the contact point is located between electron and hole pockets. The green and blue lines are the border of the electron and hole pockets. Figure from Reference [3].

For instance, in-situ electron doping using an alkaline have been introduced in 3D Dirac Semimetals Cd_3As_2 to tune the position of the Fermi energy [13]. Besides, changing the Fermi level position in Cd_3As_2 via electrostatic doping by solid electrolyte gating have been reported [42]. However, to achieve the potential barrier with the second method the material is needed to be thin (in the dimension of nanometer) since the screening effect is available only for short distances [2]. In addition, carrier concentration can be altered by applying gate-voltage and it has been realised in Type-II Weyl semimetal WTe_2 [43].

Non-tilted Weyl fermions can be described by the low-energy Hamiltonian (2.14). Without loss of generality we consider Weyl fermions around one node. By solving the eigenvalue equation $[\mathcal{H}]\{\xi\} = \mathcal{E}_F\{\xi\}$ we get the eigenenergies

$$\mathcal{E}_F - V_0 = \pm\hbar v_F k_F. \tag{2.19}$$

In order to investigate the transport properties one can make the ansatz

$$\psi(x, y, z) = \phi(y)e^{ik_x x}e^{ik_z z} \tag{2.20}$$

since the transverse wave vectors k_x and k_z are conserved throughout the motion. By assuming a transmission of electrons along x direction at the azimuthal angle ϕ with respect to the x-axis and the angle θ between $\mathbf{k}$ and xy-plane, the components of the eigenstates of the Hamiltonian (2.14) can be obtained as

$$\psi = \begin{bmatrix} \psi_1 \\ \psi_2 \end{bmatrix} = \frac{1}{\sqrt{2}} \begin{bmatrix} 1 \\ e^{i\phi} \sec\theta(\pm 1 - \sin\theta) \end{bmatrix} e^{i\mathbf{k}\cdot\mathbf{r}}. \tag{2.21}$$

The positive direction for the angle θ is chosen as stated for the figures representing 3D transmission profiles to be more analyzable. The top component of the wave function ψ can be written as

$$\psi_1 = \frac{1}{\sqrt{2}} \begin{cases} (e^{ik_y y} + re^{-ik_y y})e^{ik_x x}e^{ik_z z}, & y < 0 \\ ae^{iq_y y} + be^{-iq_y y}e^{ik_x x}e^{ik_z z}, & 0 < y < L\ \cdot \\ te^{ik_y y}e^{ik_x x}e^{ik_z z}, & y > L \end{cases} \tag{2.22}$$

Assuming the Fermi energy to be positive, one can obtain the bottom component of the wave function ψ with the help of Equation 2.21

$$\psi_2 = \frac{1}{\sqrt{2}} \begin{cases} \sec\theta(1 - \sin\theta)(e^{i\phi}e^{ik_y y} + re^{-i\phi}e^{-ik_y y})e^{ik_x x}e^{ik_z z}, & y < 0 \\ \sec\alpha(s' - \sin\alpha)(e^{i\gamma}ae^{iq_y y} + e^{-i\gamma}be^{-iq_y y})e^{ik_x x}e^{ik_z z}, & 0 < y < L\ \cdot \\ e^{i\phi}\sec\theta(1 - \sin\theta)te^{ik_y y}e^{ik_x x}e^{ik_z z}, & y > L \end{cases} \tag{2.23}$$

The components of the wave vector $\mathbf{k}$ outside the barrier can be written as $k_x = k_F \cos\phi \cos\theta$, $k_y = k_F \sin\phi \cos\theta$, and $k_z = k_F \sin\theta$ where the Fermi wave vector is $k_F = \sqrt{k_x^2 + k_y^2 + k_z^2}$. Within the barrier, y-component of the wave vector is given by $q_y = \sqrt{(\frac{\mathcal{E}_F - V_0}{\hbar v_F})^2 - k_x^2 - k_z^2}$ and the propagating angles are defined by $\gamma = \tan^{-1}(\frac{q_y}{k_x})$ and $\alpha = \tan^{-1}(\frac{k_z}{q_y} \sin\gamma)$. The transmission amplitude t and, accordingly, the transmission probability $T = |t|^2$ can be derived by the conservation of transverse wave vectors in x and z-direction at the barrier interfaces $y = 0$ and $y = L$. The angular dependence of T is analyzed in Figure 2.7 in the case of constant Fermi energy $\mathcal{E}_F \approx 83$ meV and different barrier height (a,b) $V_0 = 200$, (c,d) $V_0 = 166$, and (e,f) V_0= 63 meV. (c,f) show that only normally incident electrons can be transmitted through the barrier when the applied potential is closed to the Fermi level. (a,c,e) represent the cross section of three dimensional transmissions (right plots) in the case of θ=0. Moreover, normally incident electrons can tunnel through the barrier independently of the applied potential. This unimpeded penetration can be understood with the following argument: an incident particle with the proper angle propagates through the repulsive potential by turning into its antiparticle owing to the conservation of pseudo-spin.

Furthermore, the perfect transmission angles can be provided by the resonance conditions

$$q_y = \sqrt{\left(\frac{\mathcal{E}_F - V_0}{\hbar v_F}\right)^2 - k_F^2 \cos^2\phi \cos^2\theta - k_F^2 \sin^2\theta} = \frac{n\pi}{L}, \quad n = 0, \pm 1, \pm 2 \ldots \qquad (2.24)$$

Every incident angles satisfying the condition 2.24 cause a unit transmission probability. The angles θ and ϕ, which satisfy the resonance condition (2.24) in 3D Weyl semimetals, provide perfect transmission rings instead of transmission points [2]. Since q_y is a function of the applied voltage V_0 and the Fermi energy $\mathcal{E}_F$ as shown in Equation 2.24 the shape of transmission rings is dependent on V_0 and $\mathcal{E}_F$. As one can see in Figure 2.8 the transmission rings vary with the barrier length L at constant potential and Fermi energy. When the barrier length is large enough, the transmission rings become more interesting and enjoyable.

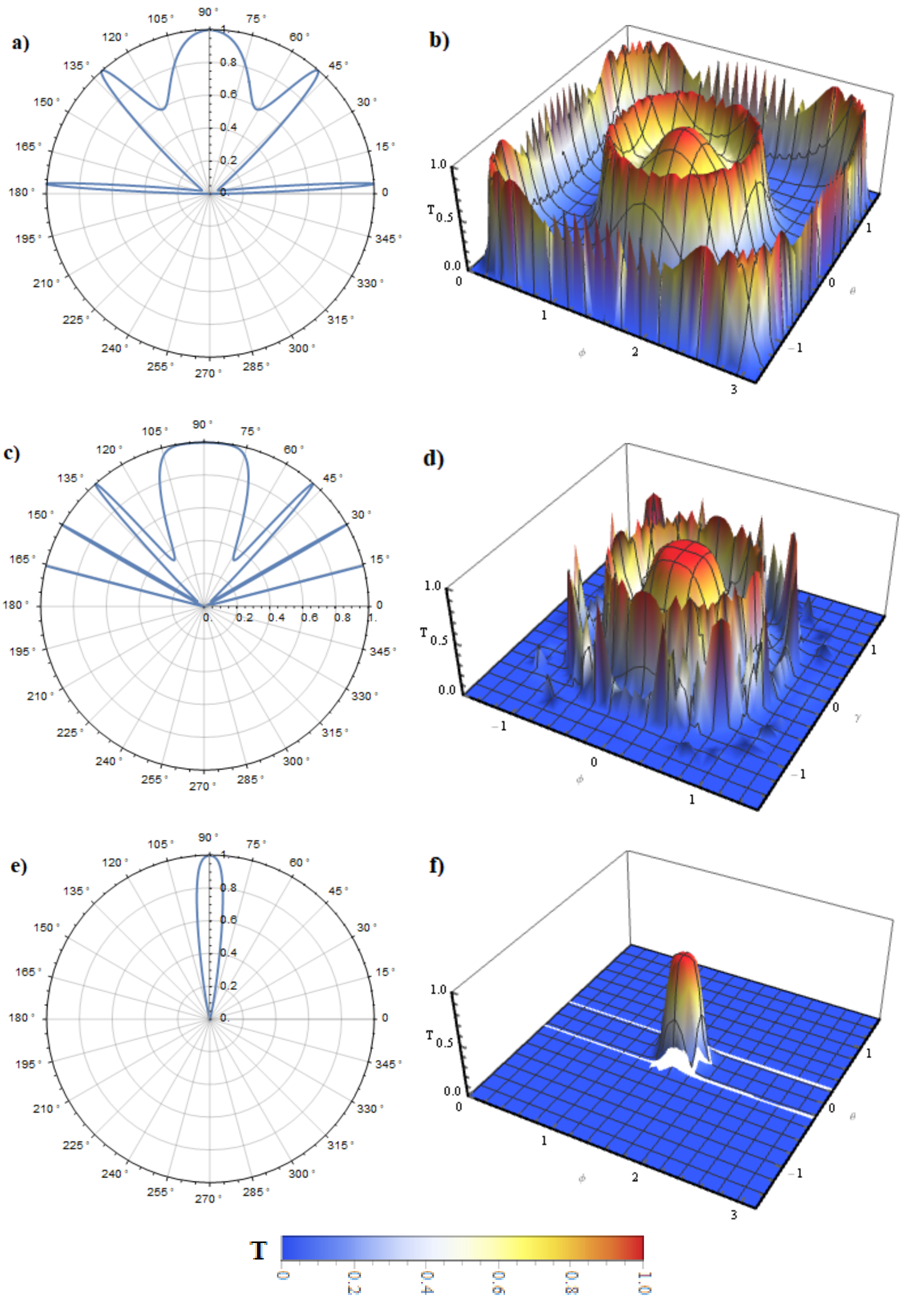

Figure 2.7. Klein tunnelling in Weyl semimetal systems. Angular dependence of transmission probability through a 100-nm-wide barrier as a function of incident angles in different configurations of potential barrier. The figure is a reproduction of the result previously presented in Reference [2].

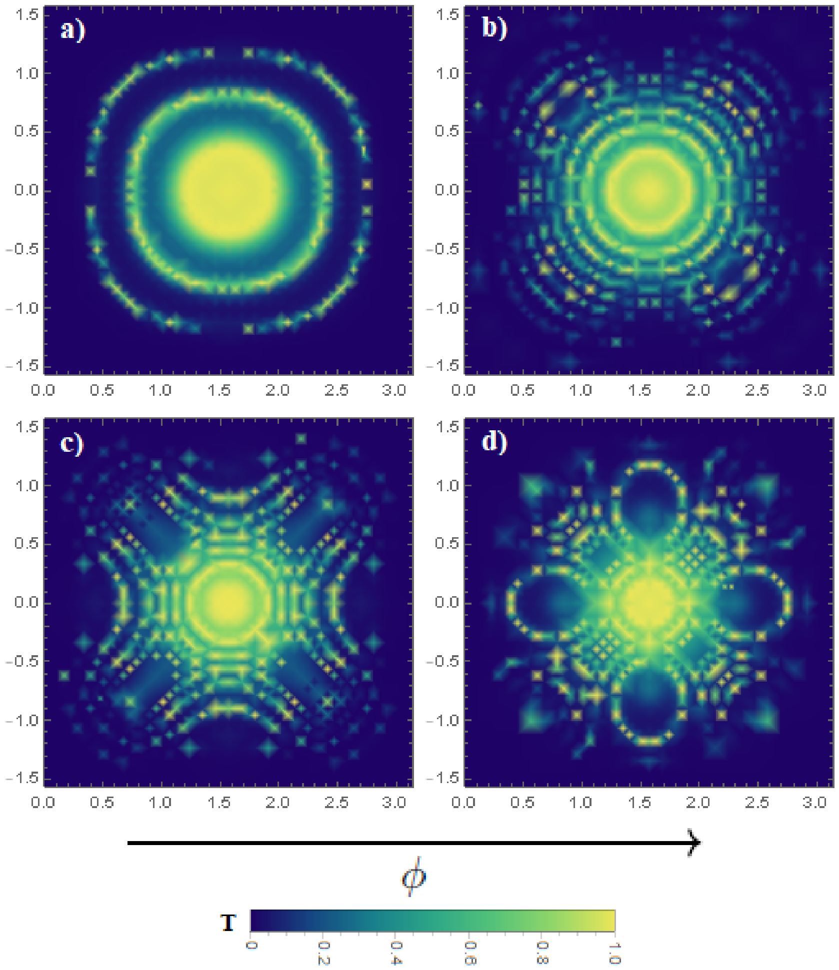

Figure 2.8. Density plots for transmission probability in the case of $\mathcal{E}_F \approx 82$ meV and applied potential $V_0 = 170$ meV. a,b,c) and d) are obtained in the case of the barrier length $L = 100$, $L = 300$, $L = 500$, and $L = 700$ nm, respectively. The vertical axis is θ-axis. The figure is a reproduction of the result previously presented in Reference [2].

The transmission of pseudo-relativistic fermions through high potential barriers has been investigated in Dirac and Weyl semimetals. Due to the chiral nature of particles in these semimetals even if the potential barrier is infinitely high, normally incident fermions can penetrate through the barrier. The absence of normal backscattering has also been examined in both Dirac and 3D Weyl semimetals multiple quantum barrier structures [44, 45]. Yeşilyurt *et al.* have been presented chiral tunnelling in Weyl semimetals with or without magnetic field and they have revealed the perfect transmission rings [2].

To analyse transmission of fermions in WSs in depth, we continue with the example of chiral tunnelling in tilted 3D WSs under the case of an electrostatic potential applied on y-axis $V(y) = V_0[\Theta(y) - \Theta(y - L)]$. We assume the Weyl cone is tilted along the x-direction. This assumption is not unrealistic. In general, energy dispersion around a Weyl point is tilted and the tilt strength is dependent on material. For example, tilt strength in NbAs and TaP are estimated by first principle calculation as $\sim 0.1 v_F$ and $\sim 0.3 v_F$ [25], respectively. Also, in quasi-2D conductor α-(BEDT-TTF)$_2$I$_3$ the tilt strength along x-direction is calculated as $\sim$ -0.8v_F under ambient pressure [5]. Consider the Weyl Hamiltonian (2.17) describing tilted Weyl fermions. The energy dispersion relation is given by

$$\mathcal{E}_F = V_0 \pm \hbar k_f v_F + \hbar k_F \cos\theta \cos\phi w_x \tag{2.25}$$

where we assume the velocities are symmetric and equal to the Fermi velocity v_F. By considering ϕ as the azimuthal angle with respect to x axis and θ as the angle between xy plane and $\mathbf{k_F}$, the Fermi wave vector is

$$k_F = \frac{\mathcal{E}}{\hbar v_F + \hbar \cos\theta \cos\phi w_x}.$$

The eigenfunctions of the Weyl Hamiltonian (2.17) are identical with the eigenfunctions (2.21) of the non-tilted Weyl Hamiltonian (2.14). This means that they are independent of the tilt parameter w in appearance.

The wave functions ψ_1 and ψ_2 are the same as in Equation 2.22 and Equation 2.23. Within the barrier the y-component of the wave vector is given by

$$q_y(w_x) = \sqrt{\frac{(\mathcal{E} - V_0 - \hbar w_x k_x)^2}{\hbar^2 v_F^2} - k_x^2 - k_z^2}.$$

At the barrier interfaces the transverse wave vectors k_x and k_z are conserved. The transmission profile is shown in Figure 2.9 and Figure 2.10 in the case of constant Fermi energy $\mathcal{E}_F \approx 82$ meV, $w_x = 0.1 v_F$, and different electrostatic potential V_0. In Figure 2.9 plots in the first row (a,d) show the angular dependence of tunnelling probability under the case of electric potential $V_0 = 200$ meV, while the ones in the second and the last row show transmission profile under the influence of applied potential $V_0 = 280$ meV and $V_0 = 480$ meV, respectively. As shown in Figure 2.8 transmission profile of non-tilted Weyl semimetals is symmetric with respect to $\phi = 0$ and $\theta = \frac{\pi}{2}$ in the presence of potential barrier. The existence of tilt parameter w breaks this symmetry as can be seen in Figure 2.10. Yeşilyurt *et al.* have recently shown that the existence of the tilt in the energy dispersion of 3D Weyl Semimetals lead to asymmetric reflection, i.e. the transmission angles are shifted along the tilt direction [25]. Graphene and 3D non-tilted Weyl Semimetals do not show this asymmetric transmission profile since the touching points reside at the high-symmetry points K and K$^{'}$ as discussed in Subsection 3.1.4. It follows from that in 3D tilted Weyl semimetals Weyl points locate at the low-symmetry k-points.

It is shown in Figure 2.10 that the perfect transmission rings are deflected in the presence of tilt velocity. We meet similar deflected transmission profile again under a delta-function magnetic field stems from magnetic stripes on top and side surfaces of the central region of a non-tilted Weyl semimetal as shown in Figure 2.11.

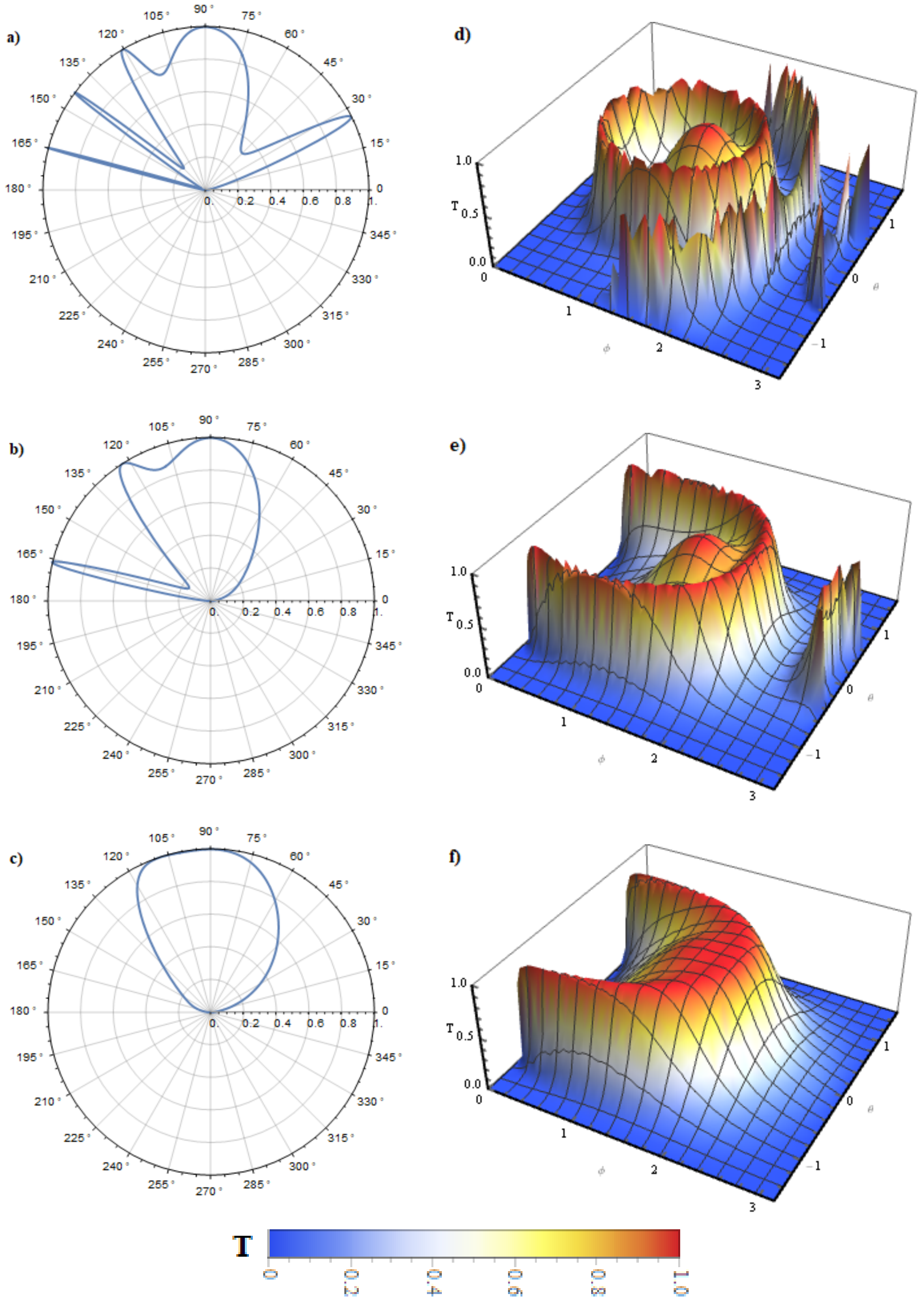

Figure 2.9. Klein tunnelling in tilted Weyl semimetal systems. Fermi energy $\mathcal{E}_F \approx 82$ meV, the barrier length $L = 100$ nm, and the tilt strength are assumed to be $w_x = 0.1 v_F$ for all configuration. (a,b,c) show the cross section of 3D transmission (d,e,f) under the same system configurations in the case of $\theta = 0$.

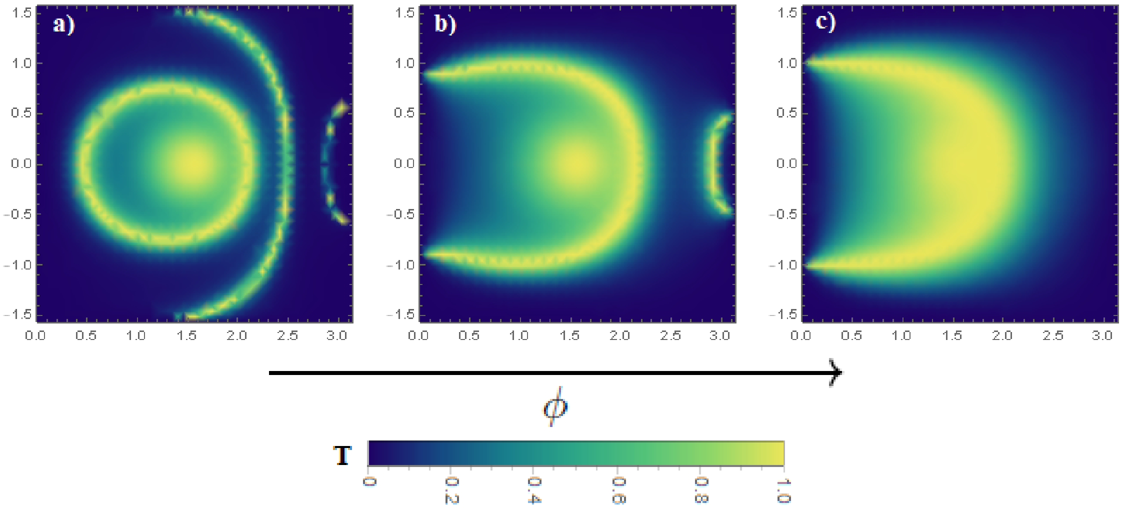

Figure 2.10. Klein tunnelling in tilted Weyl semimetal systems with $w_x = 0.1v_F$ in the case of constant barrier length $L = 100$ nm, $\mathcal{E}_F = 82.9$ meV for different configurations of the potential barrier height a)$V_0 = 200$ meV, b)$V_0 = 280$ meV, and c)$V_0 = 480$ meV, respectively. The vertical axis is θ-axis.

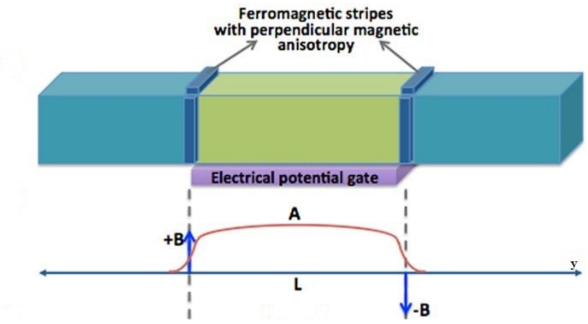

Figure 2.11. Weyl semimetal with magnetic barrier induced by ferromagnetic (FM) layers placed on top and side surfaces of the central region. The bottom figure demonstrates magnetic field induced by the ferromagnetic layer. Figure from Reference [2].

These asymmetric ferromagnetic stripes create square shaped gauge vector potential on x and z-axis

$$\begin{aligned} A_z &= B_{0z} l_B [\Theta(y) - \Theta(y-L)] \\ A_x &= B_{0x} l_B [\Theta(y) - \Theta(y-L)] \end{aligned} \tag{2.26}$$

where $l_B = \sqrt{\frac{\hbar}{|e|B_0}}$. This vector potential cause a change in the transverse wave vectors along x and z- direction and they can be rewritten as

$$\begin{aligned} k_x &= \frac{\mathcal{E}_F \cos\phi \cos\theta}{\hbar v_F} + \mu\sqrt{\frac{|B_{0x}||e|}{\hbar}} \\ k_z &= \frac{\mathcal{E}_F \sin\theta}{\hbar v_F} + \mu\sqrt{\frac{|B_{0z}||e|}{\hbar}}. \end{aligned} \tag{2.27}$$

Analysing transmission profiles shown in Figure 2.12, the magnetic barrier breaks the angular symmetry of transmission probability via transverse Lorentz displacement [2]. The examples (a) and (b) show the angular dependence of the transmission probability in the case of $V_0 = 200$ meV and $V_0 = 250$ meV, respectively. Moreover, the graphs (c) and (d) display the effect of magnetic field on normally incident electrons under barrier height $V_0 = 63$ meV and $V_0 = 75$ meV, respectively. If one set an electrostatic potential close to the Fermi energy, only normally incident electrons can penetrate the barrier as shown in Figure 2.7(e). By means of tuning the gauge vector potential, any incident wavevector can be chosen for perfect transmission. Also this allows one to shift the perfect transmission angles to different orientations as seen in Figure 2.12(c)-(d). Furthermore, one can change the radius of the perfect transmission spot by means of changing the difference between electric potential and Fermi energy.

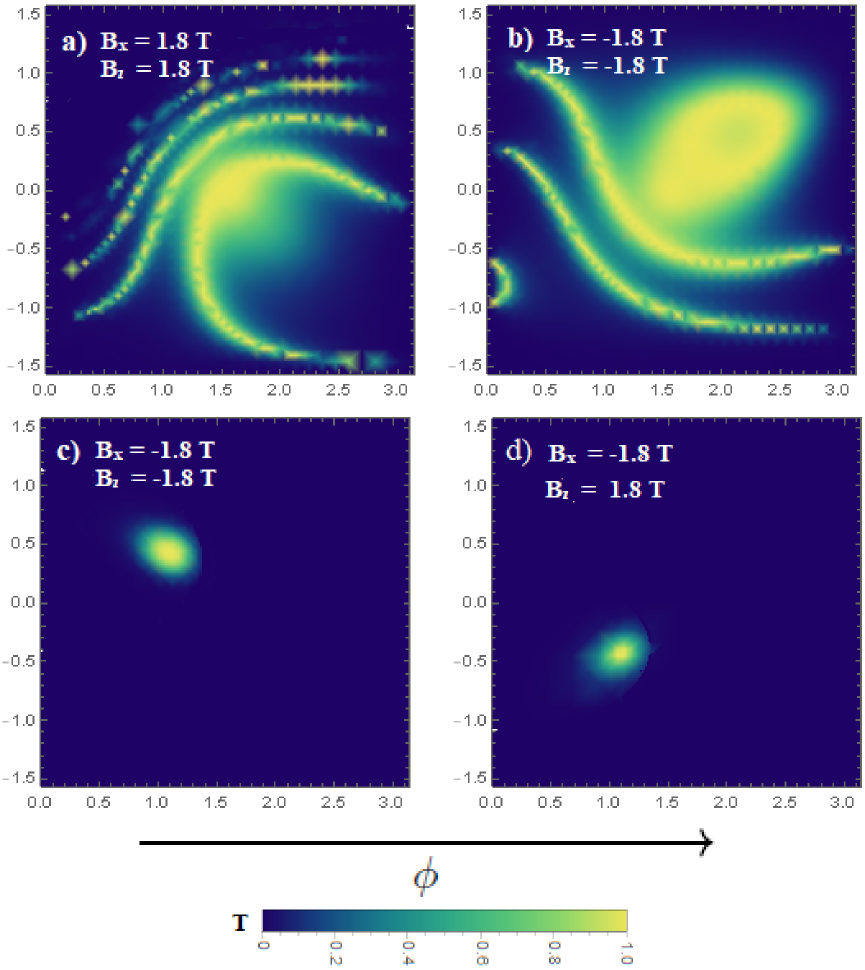

Figure 2.12. Density plots for transmission probability of quasiparticles in non-tilted Weyl semimetals in the case of constant barrier length $L = 100$ nm, $\mathcal{E}_F = 82.9$ meV for different configurations of the potential barrier height. The vertical axis is θ-axis. The figure is a reproduction of the result previously presented in Reference [2].

3. KLEIN TUNNELING IN AN ORGANIC COMPOUND: α-ET$_2$I$_3$

3.1. The Organic Compound α-(BEDT-TTF)$_2$I$_3$

The quasi-2D organic compound α-(BEDT-TTF)$_2$I$_3$ is an element of ET$_2$I$_3$ class whose molecular structure can be seen in Figure 3.1. ET molecule is roughly flat and it can be stacked in solid form in a variety of arrangements [46]. In this organic molecule, two ET molecules donate an electron to I$_3$. I$_3$ molecule is an anion due to its negative charge. Thus, ET$_2$I$_3$ is a charge-transfer salt. The members of this family differ from each other in the arrangements and orientations of ET-molecules. This difference causes diversity in the transport phenomena. α phase of ET$_2$I$_3$ molecule displays anomalous transport phenomena due to its unique features. Here α denotes the packing arrangement of the donor molecules. This system exhibits the characteristic properties of zero-gap conductors with Dirac cone. To clarify this statement we consider the following features. First of all, the number of charge carriers n per unit area of α-(BEDT-TTF)$_2$I$_3$ increases with the temperature according to $n \propto T^2$ which can be obtained by

$$\begin{aligned} n(T) &= \int_0^\infty D(E) f_0(E) dE \\ &= \int_0^\infty \frac{2|E|}{\pi \hbar^2 \bar{v}_F^2} f_0(E) dE \\ &= \frac{\pi k_B^2}{6\hbar^2 \bar{v}_F^2} T^2 \end{aligned} \tag{3.1}$$

where $f_0(E) = \frac{1}{\exp[(\mathcal{E}-\mathcal{E}_F)/k_B T]+1}$ is the Fermi distribution function, $D(E)$ is the density of states per unit area given by $D(E) = \frac{2}{\pi}\frac{|E|}{\hbar^2 \bar{v}_f^2}$ and $\bar{v}_F$ is the averaged value of the Fermi velocity [4]. In this evaluation the Fermi energy is taken to be zero since it is placed at the contact point and it is assumed to be independent of the temperature.

The number of charge carriers n per unit volume is, then,

$$n(T) = \frac{\pi k_B^2}{6c\hbar^2 \bar{v}_F^2} T^2 \tag{3.2}$$

where $c = 10.75$ Å is the lattice constant along the direction normal to the 2D plane [4].

Secondly, each conductive layers can be considered as almost independent since they are separated by the insulating layers as shown in Figure 3.1.

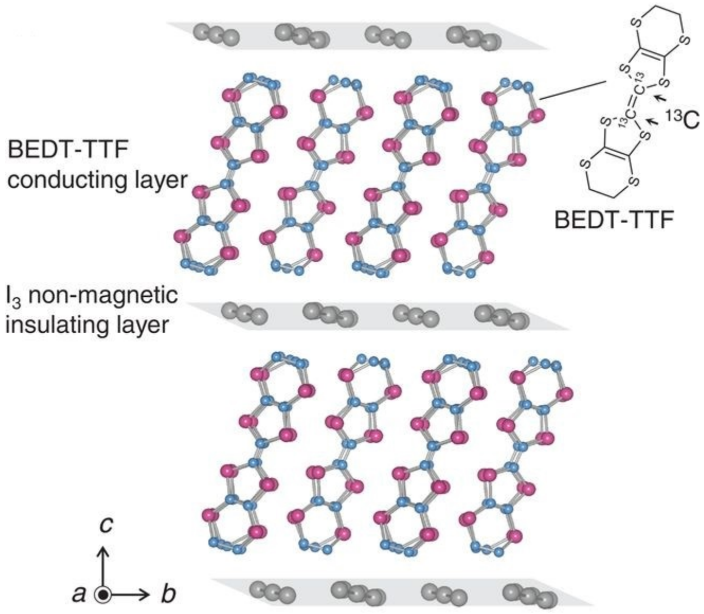

Figure 3.1. Crystal structure of α-(BEDT-TTF)$_2$I$_3$. Figure from Reference [4].

Thus, the term "sheet" resistance is valid for this system and it depends very weakly on temperature for above 7 K. It is approximately equal to the quantum resistance $R = g\frac{h}{e^2}$ with $g \backsimeq 1$. For this organic compound the parameter g is nearly constant as shown in Figure 3.2. Hence, the constant sheet resistance observed in this quasi 2D material is attributed to a zero-gap energy structure [4].

Furthermore, while the carrier density is 10^8 cm^{-2}/sheet at 2 K, the mobility of charge carriers at the same temperature is as high as 10^5 cm^{2}Vs^{-1} which is shown in Figure 3.2, 3.3 [4]. So, in the lowest-temperature regime the system has large mobility and low carrier density.

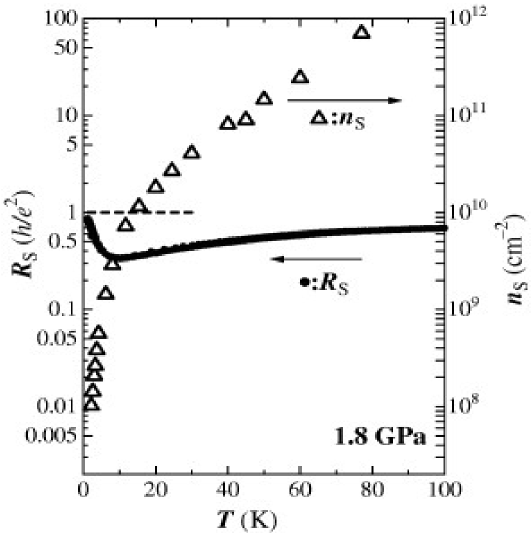

Figure 3.2. Temperature dependence of the sheet resistance R_s and charge carrier density n_s. The data plotted by black dots represent the electrical resistance. This data include a systematic error within a factor of 2. The triangles denote the number of carriers per unit area. Figure from Reference [4].

These properties are the characteristics of the 2D massless Dirac fermions. At the same time with the experimental discovery of the existence of massless DFs in graphene [32, 34] the new type of DFs was discovered in α-(BEDT-TTF)$_2$I$_3$ under high pressure [47]. This organic compound is the first layered zero-gap conductor with a tilted anisotropic Dirac cone. In addition to having zero-gap state under the change of pressure or temperature, α-(BEDT-TTF)$_2$I$_3$ displays various electronic states such as charge ordering, charge disproportionation, Mott insulator, and superconductivity with the critical temperature T_c = 7 K [5, 47]. It has attracted considerable attention among many salts due to the phase diagram involving these unconventional states which can be seen in Figure 3.4. The Dirac state of this organic oonductor differs from the conventional Dirac fermions such as graphene, bismuth, HgTe due to its two-dimensional layered structure and unique features [5].

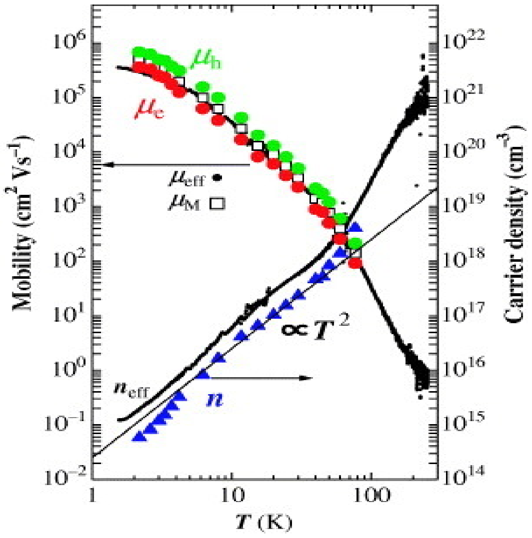

Figure 3.3. Temperature dependence of carrier density and mobility. The curves formed by black dots represent the effective mobility μ_{eff} and the number of charge carriers per volume n_{eff}. The blue triangles denote the real charge density n. Figure from Reference [4].

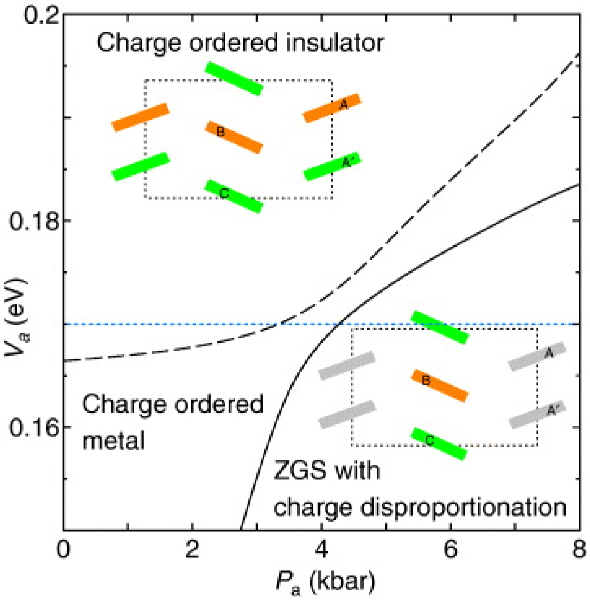

Figure 3.4. Phase diagram of α-(BEDT-TTF)$_2$I$_3$ with $U = 0.4$, $V_b = 0.05$ and $T = 0$. The solid line represents the boundary between Zero-gap state and charge-ordered metal. The dashed lines denote the boundary between charge-orders metal and the charge-ordered insulator. Figure from Reference [5].

This section is organized as follows. The two-dimensional electronic system and the extended Hubbard model with on-site and nearest-neighbour interaction is described in Subsection 3.1.1 and afterwards ZGS is examined. Subsequently in Subsection 3.1.2 we examine Klein tunnelling in α-(BEDT-TTF)$_2$I$_3$ theoretically.

3.1.1. Electronic States Under Uniaxial Pressure of α-(BEDT-TTF)$_2$I$_3$

A two-dimensional lattice structure of α-(BEDT-TTF)$_2$I$_3$ which consists of 4 ET molecules per unit cell is shown in Figure 3.5. The notations c_1, c_2, c_3, p_1, p_2, p_3, and p_4 in Figure 3.5 denote the nn and c_1', c_3', and c_4' represent the nnn electron hopping. The anions which form a layer between conductive layers are shown by dashed rectangles. The sites of the unit cell A(= A$^{'}$), B, and C are inequivalent in contrast with the model for the electronic system of graphene. The tight-binding Hamiltonian with the on-site and nearest-neighbour interaction is given by

$$\begin{aligned}\mathcal{H} = &\sum_{(i\alpha;j\beta),\sigma} (t_{i\alpha;j\beta} a^{\dagger}_{i\alpha\sigma} a_{j\beta\sigma} + h.c.) + \sum_{i\alpha} U a^{\dagger}_{i\alpha\uparrow} a^{\dagger}_{i\alpha\downarrow} a_{i\alpha\downarrow} a_{i\alpha\uparrow} \\ &+ \sum_{(i\alpha;j\beta)} \sum_{\sigma,\sigma'} V_{\alpha,\beta} a^{\dagger}_{i\alpha\sigma} a^{\dagger}_{j\beta\sigma'} a_{j\beta\sigma'} a_{i\alpha\sigma} + \sum_{i\alpha,\sigma} I_\alpha a^{\dagger}_{i\alpha\sigma} a_{i\alpha\sigma}\end{aligned} \tag{3.3}$$

where i and j represent the sites of the unit cell and run from 1 to the number of the unit cell of the square lattice. α and β are indices of ET sites A(= A$^{'}$), B, C of the unit cell [5]. I_α represents the local potential, which comes from the anion, at the sites $\alpha = 1, \cdots, 4$ and $t_{i\alpha;j\beta}$ denotes the transfer energy from the site (j, β) to the site (i, α). The transfer energies are highly anisotropic as will be seen later in this subsection. $a^{\dagger}_{i\alpha\sigma}$ and $a_{i\alpha\sigma}$ are creation and annihilation operators with σ denoting the spin of the electron, respectively. Lastly, U and $V_{\alpha\beta}$ denote the on-site and the nearest-neighbour repulsive interaction. We use V_c for c_1, c_2, and c_3 bonds and V_p for p_1, p_2, p_3, and p_4 bonds.

From now on, the effect of the anion potential I_α is ignored [5]. Also, the repulsive interactions can be disregarded since zero-gap state exists under the case of $U = V_c = V_p = 0$ as well, as noted in references [9, 48, 49].

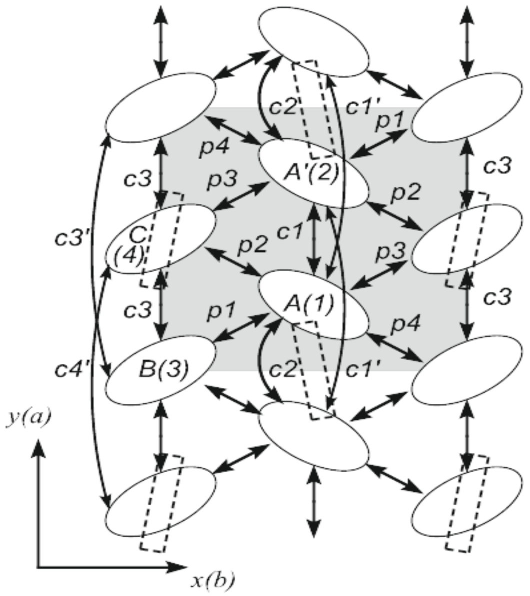

Figure 3.5. Lattice structure of the conducting plane of α-(BEDT-TTF)$_2$I$_3$. Figure from Reference [6].

The Fourier transform of the annihilation operator $a_{i\alpha}$ is

$$a_{i\alpha} = \frac{1}{\sqrt{N}} \sum_{\mathbf{k}} a_{\mathbf{k}\alpha} e^{i\mathbf{k}\cdot\mathbf{r}_i} \tag{3.4}$$

where N is the number of unit cells. Then, the nearest-neighbour part of the Hamiltonian (3.3) is rewritten as

$$\begin{aligned}
\mathcal{H} &= \sum_{\alpha,\beta}\sum_{i,j}\sum_{\mathbf{k},\mathbf{q},\sigma} \frac{1}{N} t_{i\alpha:j\beta} a^{\dagger}_{\mathbf{k}\alpha\sigma} a_{\mathbf{q}\beta\sigma} e^{-i\mathbf{k}\cdot\mathbf{r}_i} e^{i\mathbf{q}\cdot\mathbf{r}_j} \\
&= \frac{1}{N}\sum_{\alpha,\beta}\sum_{i,j}\sum_{\mathbf{k},\sigma} t_{i\alpha;j\beta} a^{\dagger}_{\mathbf{k}\alpha\sigma} a_{\mathbf{k}\beta\sigma} e^{i\mathbf{k}\cdot(\mathbf{r}_j-\mathbf{r}_i)} \\
&= \sum_{\alpha,\beta}\sum_{\mathbf{k},\sigma} a^{\dagger}_{\mathbf{k}\alpha\sigma} \frac{1}{N} \sum_{i} \left\{ \sum_{j} t_{i\alpha,j\beta e^{i\mathbf{k}\cdot(\mathbf{r}_j-\mathbf{r}_i)}} \right\} a_{\mathbf{k}\beta\sigma} \\
&= \sum_{\alpha,\beta}\sum_{\mathbf{k},\sigma} a^{\dagger}_{\mathbf{k}\alpha\sigma} \frac{1}{N} \sum_{i} \left\{ t_{i\alpha,i\beta} + \sum_{j\neq i} t_{i\alpha;j\beta} e^{i\mathbf{k}\cdot(\mathbf{r}_j-\mathbf{r}_i)} \right\} a_{\mathbf{k}\beta\sigma} \\
&= \sum_{\alpha,\beta}\sum_{\mathbf{k},\sigma} a^{\dagger}_{\mathbf{k}\alpha\sigma} \frac{1}{N} \left\{ N t_{\alpha,\beta} + \sum_{j\neq 1} t_{1\alpha;j\beta} e^{i\mathbf{k}\cdot(\mathbf{r}_j-\mathbf{r}_1)} + \cdots \sum_{j\neq N} t_{1\alpha;j\beta} e^{i\mathbf{k}\cdot(\mathbf{r}_j-\mathbf{r}_N)} \right\} a_{\mathbf{k}\beta\sigma}
\end{aligned} \tag{3.5}$$

Herein, we remind that we consider only the transfer energies between nearest-neighbour sites. This approximation provides that in each summation over j in the last line of Equation 3.5 all elements except the ones representing the nearest-neighbour are zero, i.e.

$$\sum_{j \neq i} t_{i\alpha;j\beta} e^{i\mathbf{k}\cdot(\mathbf{r}_j - \mathbf{r}_i)} = \sum_{\boldsymbol{\delta}} t_{\alpha,\beta} e^{i\mathbf{k}\cdot\boldsymbol{\delta}}, \quad i = 1, 2, \ldots, N \tag{3.6}$$

where $\boldsymbol{\delta} = \mathbf{r}_j - \mathbf{r}_i$ is the vector representing the nearest-neighbour of ith unit cell. With the help of the above equation, we obtain the following

$$\begin{aligned} H &= \sum_{\alpha,\beta} \sum_{\mathbf{k},\sigma} a^{\dagger}_{\mathbf{k}\alpha\sigma} \left\{ t_{\alpha,\beta} + \sum_{\boldsymbol{\delta}} t_{\alpha,\beta} e^{i\mathbf{k}\cdot\boldsymbol{\delta}} \right\} a_{\mathbf{k}\beta\sigma} \\ &= \sum_{\alpha,\beta} \sum_{\mathbf{k},\boldsymbol{\delta},\sigma} a^{\dagger}_{\mathbf{k}\alpha\sigma} t_{\alpha\beta} e^{i\mathbf{k}\cdot\boldsymbol{\delta}} a_{\mathbf{k}\beta\sigma} \\ &= \sum_{\alpha,\beta} \sum_{\mathbf{k},\sigma} a^{\dagger}_{\mathbf{k}\alpha\sigma} \epsilon_{\alpha\beta}(\mathbf{k}) a_{\mathbf{k}\beta\sigma} \end{aligned} \tag{3.7}$$

where $\epsilon_{\alpha,\beta} = t_{\alpha,\beta} \sum_{\delta} e^{i\mathbf{k}\cdot\boldsymbol{\delta}}$. Equation 3.7 can be rewritten as

$$\mathcal{H} = \sum_{\mathbf{k},\sigma} \begin{pmatrix} a^{\dagger}_{\mathbf{k}1\sigma} & a^{\dagger}_{\mathbf{k}2\sigma} & a^{\dagger}_{\mathbf{k}3\sigma} & a^{\dagger}_{\mathbf{k}4\sigma} \end{pmatrix} T(\mathbf{k}) \begin{pmatrix} a_{\mathbf{k}1\sigma} \\ a_{\mathbf{k}2\sigma} \\ a_{\mathbf{k}3\sigma} \\ a_{\mathbf{k}4\sigma} \end{pmatrix} \tag{3.8}$$

where $T(\mathbf{k})$ can be expressed [6] as

$$T(\mathbf{k}) = \begin{bmatrix} 0 & t_{c1} + t_{c2}e^{-ik_y} & t_{p1} + t_{p4}e^{ik_x} & t_{p2} + t_{p3}e^{ik_x} \\ t_{c1} + t_{c2}e^{ik_y} & 0 & t_{p4}e^{ik_y} + t_{p1}e^{i(k_x+k_y)} & t_{p3} + t_{p2}e^{ik_x} \\ t_{p1} + t_{p4}e^{-ik_x} & t_{p4}e^{-ik_y} + t_{p1}e^{-i(k_x+k_y)} & 0 & t_{c3} + t_{c3}e^{-ik_y} \\ t_{p2} + t_{p3}e^{-ik_x} & t_{p3} + t_{p2}e^{-ik_x} & t_{c3} + t_{c3}e^{ik_y} & 0 \end{bmatrix}. \tag{3.9}$$

The hopping integrals are evaluated from the first-principle density functional calculation at 8 K under ambient pressure and are given by $t_{c1} = -0.0511$, $t_{c2} = 0.0323$, $t_{c3} = -0.0267$, $t_{p1} = 0.1296$, $t_{p2} = 0.1241$, $t_{p3} = 0.0152$, and $t_{p4} = 0.0513$ in units of eV [9]. The details of the transfer integrals under different pressure conditions are given in Table C.1 in Appendix C. The transfer energies are pressure-dependent and can be determined by the extrapolation formula

$$\begin{aligned} t_{c_i}(P_a) &= t_{c_i}(1 + K_{c_i}P_a), \quad i = 1,2,3,4 \\ t_{p_j}(P_a) &= t_{p_j}(1 + K_{p_j}P_a), \quad j = 1,2,3 \end{aligned} \tag{3.10}$$

where $t_{c_i(p_j)}(P_a)$ denotes the transfer energy under uniaxial pressure P_a along the a-axis [5]. The coefficients $K_{c_i(p_j)}$ and $t_{c_i(p_j)}$ are estimated by using the data of α-(ET)$_2$I$_3$ under various pressure conditions [5] and can be seen in Table C.2 in Appendix C. The eigenvalue equation for the Hamiltonian (3.8) is

$$\sum_{\beta=1}^{4} \epsilon_{\alpha\beta\sigma}(\mathbf{k})\psi_{\gamma\beta\sigma}(\mathbf{k}) = \xi_{\gamma\sigma}\psi_{\gamma\alpha\sigma}(\mathbf{k}), \quad \alpha = 1,2,3,4 \tag{3.11}$$

where $\gamma = 1, \cdots, 4$, $\xi_{\gamma\sigma}$ denote the energy eigenvalues and $\psi_{\gamma\sigma} = [\psi_{\gamma 1}, \psi_{\gamma 2}, \psi_{\gamma 3}, \psi_{\gamma 4}]$ is the corresponding wave function for an electron with spin σ. The eigenvectors have 4 components of respective sites where, as is stated, two of them are equivalent sites and the others correspond to the inequivalent sites. The number of electrons with spin σ on the site α is given by

$$n_{\alpha\sigma} = \langle a^{\dagger}_{i\alpha\sigma} a_{i\alpha\sigma} \rangle = \frac{1}{N} \sum_{\mathbf{k}} \sum_{\gamma=1}^{4} \psi^{*}_{\gamma\alpha\sigma}(\mathbf{k})\psi_{\gamma\alpha\sigma}(\mathbf{k}) f(\xi_{\gamma\sigma}(\mathbf{k})) \tag{3.12}$$

where $f(\xi_{\gamma\sigma}(\mathbf{k})) = \frac{1}{\exp[(\xi_{\gamma\sigma}(\mathbf{k})-\mu)/Tk_{\mathrm{B}}]+1}$ is the Fermi distribution function. The total number of electrons in one unit cell is $\sum_{\alpha\sigma} n_{\alpha\sigma} = 6$, thus the system is 3/4-filled. The chemical potential μ is determined [5] by

$$\frac{3}{2} = \frac{1}{4} \sum_{\alpha\sigma} n_{\alpha\sigma}. \tag{3.13}$$

The number of electrons in A and A' sites are equivalent, $n_1 = n_2$ where $n_\alpha = n_{\alpha\uparrow} + n_{\alpha\downarrow}$, due to inversion symmetry.

<u>3.1.1.1. Zero-Gap State.</u> As can be seen in Figure 3.4 ZGS exists under a wide range of pressure. Diagonalizing the Hamiltonian (3.8) we get 4 energy bands since a unit cell contains 4 ET sites. For the ZGS one can use only the reduced part of the 4×4 Hamiltonian (3.8), which corresponds to conduction and valence bands. The highest energy band is unoccupied whereas the second band is almost filled. Since inversion symmetry is not broken, the conduction and valence bands coincide at two distinct points $\pm\mathbf{k_D}$, in the first BZ, location of which moves continuously with the variation of hopping integrals. Zero gap structure may be related to the symmetry of materials or accidental degeneracy of the bands. In graphene, the Dirac state is caused by the symmetry of the material. In contrast to the case of graphene, the ZGS in this organic compound is related to the accidental degeneracy of the bands. Although the transfer energies, and accordingly contact points, vary with the pressure (3.10), the existence of Dirac state is independent of variation of the pressure. The 2×2 Hamiltonian can be expanded around the contact points $\pm\mathbf{k_D}$

$$\mathcal{H}(\mathbf{k}) = \mathcal{H}(\mathbf{k_D}) + (\mathbf{k} - \mathbf{k_D}) \cdot \nabla\mathcal{H}(\mathbf{k})|_{\mathbf{k}=\mathbf{k_D}}. \tag{3.14}$$

$\mathcal{H}(\mathbf{k_D}) = 0$ since the chemical potential and the Fermi energy meet at $\mathbf{k} = \pm\mathbf{k_D}$. The velocity matrix is given as $\tilde{\mathbf{v}}_{\gamma\gamma'} = \langle\psi_\gamma(\mathbf{k})|\nabla\mathcal{H}|\psi_{\gamma'}(\mathbf{k})\rangle$ where $\gamma(\gamma') = 1, 2$ denotes the conduction ($\gamma = 1$) and valence band ($\gamma = 2$). The wave function $\psi_{\gamma(\gamma')}$ stands for the expression of the eigenfunction corresponding to the eigenvalue $\xi_{\gamma(\gamma')}$. With the help of the Equation 3.14, the components of the velocity matrix is given by

$$\tilde{v}^i_{\gamma\gamma'} = \sum_{\alpha\beta} \psi^*_{\gamma\alpha}(\mathbf{k_D}) \frac{\partial\epsilon_{\alpha\beta}(\mathbf{k})}{\partial k_i}\bigg|_{\mathbf{k}=\mathbf{k_D}} \psi_{\gamma'\beta}(\mathbf{k_D}) \tag{3.15}$$

where $i = x, y$, and $\alpha, \beta = 1, 2, 3, 4$.

The Hamiltonian (3.14) can be explicitly written by substituting the components of the velocity matrix (3.15) in the expanded Hamiltonian (3.14) as

$$
\begin{aligned}
H &= \mathbf{k} \cdot \begin{bmatrix} \tilde{\mathbf{v}}_{11} & \tilde{\mathbf{v}}_{12} \\ \tilde{\mathbf{v}}_{21} & \tilde{\mathbf{v}}_{22} \end{bmatrix} \\
&= \mathbf{k} \cdot \begin{bmatrix} \mathbf{v}_0 + \mathbf{v}_3 & \mathbf{v}_1 - i\mathbf{v}_2 \\ \mathbf{v}_1 + i\mathbf{v}_2 & \mathbf{v}_0 - \mathbf{v}_3 \end{bmatrix} \\
&= \begin{bmatrix} k_x(v_{0x} + v_{3x}) + k_y(v_{0y} + v_{3y}) & k_x(v_{1x} - iv_{2x}) + k_y(v_{1y} - iv_{2y}) \\ k_x(v_{1x} + iv_{2x}) + k_y(v_{1y} + iv_{2y}) & k_x(v_{0x} - v_{3x}) + k_y(v_{0y} - v_{3y}) \end{bmatrix} \\
&= \mathbf{k} \cdot \mathbf{v}_0\sigma_0 + \mathbf{k} \cdot \mathbf{v}_1\sigma_1 + \mathbf{k} \cdot \mathbf{v}_2\sigma_2 + \mathbf{k} \cdot \mathbf{v}_3\sigma_3 \\
&= \sum_{i=0}^{3} \mathbf{k} \cdot \mathbf{v}_i\sigma_i
\end{aligned}
\tag{3.16}
$$

where the velocity vectors $\mathbf{v}_i (i = 0, 1, 2, 3)$ in different directions are defined [5] as

$$
\begin{aligned}
\mathbf{v_0} &= \frac{1}{2}(\tilde{\mathbf{v}}_{11} + \tilde{\mathbf{v}}_{22}) \\
\mathbf{v_1} &= \mathrm{Re}\tilde{\mathbf{v}}_{12} \\
\mathbf{v_2} &= -\mathrm{Im}\tilde{\mathbf{v}}_{12} \\
\mathbf{v_3} &= \frac{1}{2}(\tilde{\mathbf{v}}_{11} - \tilde{\mathbf{v}}_{22}).
\end{aligned}
\tag{3.17}
$$

The energy eigenvalues of the Hamiltonian (3.16) are

$$
\mathcal{E}_{1,2} = k_x\omega_x + k_y\omega_y \pm \sqrt{(k_xv_{1x} + k_yv_{1y})^2 + (k_xv_{2x} + k_yv_{2y})^2 + (k_xv_{3x} + k_yv_{3y})^2}. \tag{3.18}
$$

where $\mathbf{v_0} = (w_x, w_y)$.

In most of the recent studies [5,6,50] the Coulomb interactions U, V_a, and V_b are taken as $U = 0.4, V_c = 0.17$, and $V_p = 0.05$ in units of eV. This choice also gives ZGS as shown in Figure 3.4 with the contact points $\mathbf{k_D} = \pm(0.686\pi, -0.443\pi)$ [6]. Setting both primitive and the reciprocal lattice vectors to have a unit length the velocities $\mathbf{v_i}(i = 0, 1, 2, 3)$ (3.17) are calculated [6,49] as

$$\mathbf{v_0} = (-38.9, 4.8), \mathbf{v_1} = (0, -0.5), \mathbf{v_2} = (0, 43.9), \mathbf{v_3} = (51.5, 0.9) \quad \text{in meV.} \tag{3.19}$$

To obtain the velocities in dimension length/time one has to multiply the velocities either by $a/\hbar$ or $b/\hbar$ where a and b are lattice constants which are estimated as $a = 8.567$ Å and $b = 10.282$ Å under the pressure 2.3 GPa [49]. Then, the velocities can be approximately taken as

$$\mathbf{v_0} = -(w_x, 0) \quad \mathbf{v_1} = \mathbf{0} \quad \mathbf{v_2} = (0, v_y) \quad \mathbf{v_3} = (v_x, 0) \tag{3.20}$$

where $w_x \approx 0.8 \times 10^5$ ms^{-1} and $v_x \approx v_y = 1.0 \times 10^5$ ms^{-1} [47].

Around the contact point $\mathbf{k_D}$ the low energy continuum model for the organic compound is shown to be given by the generalized 2D Weyl Hamiltonian as in Equation 2.17 under ambient pressure [6,50,51]. This is achieved by using another choice of velocities, i.e. $\mathbf{v_0} = -(w_x, 0), \quad \mathbf{v_1} = (v_x, 0), \quad \mathbf{v_2} = (0, v_y), \quad \mathbf{v_3} = \mathbf{0}$. These choices are related each other by a unitary transformation [48]. In contrast to the case of graphene, the velocity of fermions along the x and y direction is slightly different.

The energy eigenvalues of the Hamiltonian 2.17 are given by

$$\mathcal{E}_1(\mathbf{k}) = \hbar w_x k_x + \hbar w_y k_y + \hbar\sqrt{v_x^2 k_x^2 + v_y^2 k_y^2} \tag{3.21}$$

and

$$\mathcal{E}_2(\mathbf{k}) = \hbar w_x k_x + \hbar w_y k_y - \hbar\sqrt{v_x^2 k_x^2 + v_y^2 k_y^2}. \tag{3.22}$$

Taking $\mathcal{E}_1$ into account, the above equation can be written in the following form

$$a_1 k_x^2 + a_2 k_y^2 + a_3 k_x k_y + a_4 k_x + a_5 k_y = 1 \tag{3.23}$$

where $a_1 = \left(\frac{v_x^2 - w_x^2}{\mathcal{E}_1^2}\right) k_x^2$, $a_2 = \left(\frac{v_y^2 - w_y^2}{\mathcal{E}_1^2}\right) k_y^2$, $a_3 = \frac{-2w_x w_y}{\mathcal{E}_1^2} k_x k_y$, $a_4 = \frac{2w_x}{\mathcal{E}_1} k_x$, and $a_5 = \frac{2w_y}{\mathcal{E}_1} k_y$. Equation 3.23 represents the general form of an ellipse with the center

$$x_0 = \frac{2a_2 a_4 - a_3 a_5}{a_3^2 - 4a_1 a_2} \quad \text{and} \quad y_0 = \frac{2a_1 a_5 - a_3 a_4}{a_3^2 - 4a_1 a_2}. \tag{3.24}$$

The angle between the major axis a' of the ellipse and k_x-axis is

$$\phi = \frac{1}{2} \arctan\left(\frac{a_3}{a_1 - a_2}\right) \tag{3.25}$$

and the semi-axis lengths are given by

$$a' = \sqrt{\frac{2(a_1 a_5^2 + a_2 a_4^2 - a_3^2 - a_3 a_4 a_5 + 4a_1 a_2)}{(a_3^2 - 4a_1 a_2)(-a_1 - a_2 + \sqrt{(a_1 - a_2)^2 + a_3^2})}} \tag{3.26}$$

and

$$b' = \sqrt{\frac{2(a_1 a_5^2 + a_2 a_4^2 - a_3^2 - a_3 a_4 a_5 + 4a_1 a_2)}{(a_3^2 - 4a_1 a_2)(-a_1 - a_2 - \sqrt{(a_1 - a_2)^2 + a_3^2})}}. \tag{3.27}$$

3.1.2. Klein Tunnelling in Quasi-2D Organic Conductor α-ET$_2$I$_3$

Consider the 2D tilted Weyl Hamiltonian

$$\mathcal{H} = \hbar \begin{pmatrix} w_x k_x & v_x k_x - i v_y k_y \\ v_x k_x + i v_y k_y & w_x k_x \end{pmatrix}. \tag{3.28}$$

Assuming a rectangular potential barrier is applied along the y-axis as in Figure 3.7, the energy dispersion relation of the Hamiltonian (3.28) is given by

$$\mathcal{E}(\mathbf{k}) - V_0 = \hbar w_x k_x + \hbar w_y k_y \pm \hbar\sqrt{v_x^2 k_x^2 + v_y^2 k_y^2}. \tag{3.29}$$

where V_0 stands for constant electric potential. The energy dispersion is strongly tilted along the x-axis as shown in Figure 3.6. Therefore, Fermi velocity is anisotropic around the cone and is expressed as

$$v_F = w_x \cos\phi + w_y \sin\phi + s\sqrt{v_x^2 \cos^2\phi + v_y^2 \sin^2\phi} \tag{3.30}$$

where $s = \pm 1$ depends on the energy eigenvalue and the angle ϕ is measured from the x-axis. In contrast to the case of graphene, the sites ($A = A', B$, and C) of the unit cell are inequivalent and the variety of hopping integrals lead to low symmetry in the crystal. The system has only inversion symmetry [49]. The tilting of Dirac cone arises from the low-symmetry and it decreases the effective velocity [51]. As explained in the last subsection we simply set w_y to 0, hereafter, to examine the chiral tunnelling in the quasi-2D organic conductor analytically.

Assume that we apply a delta function magnetic field B on y-axis, i.e., $\mathbf{B} = -B_0 l_B[\delta(y) - \delta(y - L)]\hat{z}$, which corresponds to a magnetic gauge potential $\mathbf{A} = B_0 l_B[\theta(y) - \theta(y - L)]\hat{x}$ where $l_B = \sqrt{\frac{\hbar}{|e|B_0}}$. The effective Hamiltonian is modified by the gauge potential which shifts the wave-vector

$$k_x \longrightarrow k_x + \mu\frac{e|\mathbf{A}|}{\hbar} \tag{3.31}$$

where $\mu = \pm$ denotes the sign of the magnetic field.

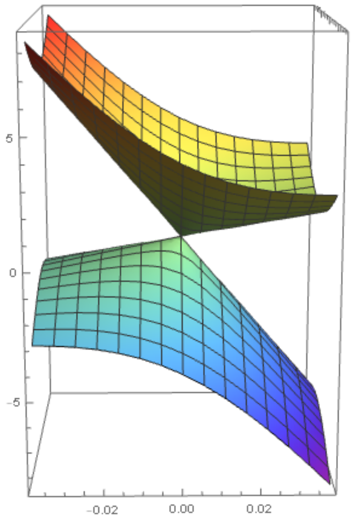

Figure 3.6. Band dispersion of α-ET$_2$I$_3$. The vertical axis represents the band energy in meV on the $k_x - k_y$ plane and $\mathcal{E}_F$ locates at the contact point. This plot is obtained under the assumptions $v_x \approx v_y = 10^5$ ms^{-1} and $w_x \approx -0.8 \times 10^5$ ms^{-1}.

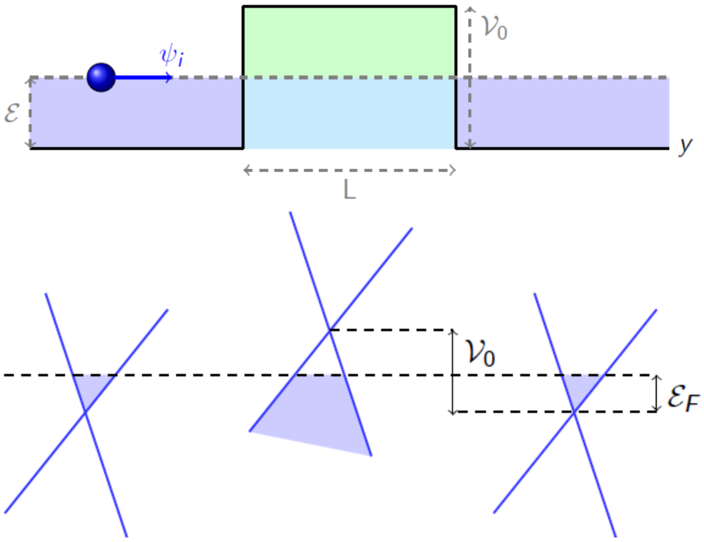

Figure 3.7. (Top) Potential barrier of height V_0 and width L. (Bottom) Low-energy spectrum for quasipaticles in α-ET$_2$I$_3$. The energy dispersion is linear up to 100 meV [5]. The three diagrams schematically show the positions of the Fermi energy $\mathcal{E}_F$ across such a barrier.

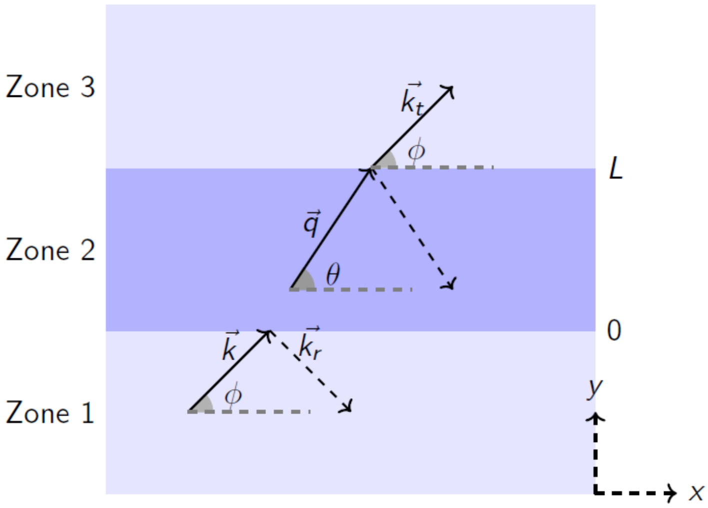

Figure 3.8. Definition of angles and the wavevectors in three zones: incident $\mathbf{k} = (k_x, k_y) = k(\cos\phi, \sin\phi)$, reflected $\mathbf{k_r} = (k_x, -k_y)$, and transmitted $\mathbf{k_t} = \mathbf{k}$.

The energy eigenvalues of the Hamiltonian (3.28) are given by

$$\mathcal{E} - V_0 = \hbar\omega_x(k_x + \mu\delta) \pm \hbar\sqrt{v_x^2(k_x + \mu\delta)^2 + v_y^2 k_y^2} \tag{3.32}$$

where $\delta = \frac{e|\mathbf{A}|}{\hbar}$ and the corresponding normalized eigenfunctions are

$$\psi_s = \begin{bmatrix} \psi_1 \\ \psi_2^s \end{bmatrix} = \frac{1}{\sqrt{2}} \begin{bmatrix} 1 \\ se^{i\phi_v} \end{bmatrix} e^{i\mathbf{k}\cdot\mathbf{r}} \tag{3.33}$$

which are independent of the tilt parameter, where ϕ_v is defined by $\phi_v \equiv \arctan(\frac{v_y k_y}{v_x k_x})$.

Then, the top component of the wave function ψ_s for incident, propagating, and transmitted regions can be written as (see Figure 3.8)

$$\psi_1 = \frac{1}{\sqrt{2}} \begin{cases} (e^{ik_y y} + re^{-ik_y y})e^{ik_x x}, & y < 0 \\ (ae^{iq_y y} + be^{-iq_y y})e^{ik_x x}, & 0 < y < L \cdot \\ te^{ik_y y}e^{ik_x x}, & y > L \end{cases} \tag{3.34}$$

Therefore, one can obtain the explicit form of the bottom component of the wave function with the help of the relation $\psi_2^s = se^{i\phi_v}\psi_1$ (3.33),

$$\psi_2 = \frac{1}{\sqrt{2}} \begin{cases} s(e^{i\phi_v}e^{ik_y y} + re^{-i\phi_v}e^{-ik_y y})e^{ik_x x}, & y < 0 \\ s'(ae^{i\theta_v}e^{iq_y y} + be^{-i\theta_v}e^{-iq_y y})e^{ik_x x}, & 0 < y < L \\ ste^{i\phi_v}e^{ik_y y}e^{ik_x x}, & y > L \end{cases} \tag{3.35}$$

where the refraction angle θ_v is defined by $\theta_v \equiv \arctan(\frac{v_y q_y}{v_x k_x})$. Outside the barrier, x and y components of the wave vector $\mathbf{k}$ are $k_x = k_f \cos\phi$ and $k_y = k_f \sin\phi$, respectively, where the Fermi wave vector is

$$k_F = \frac{\mathcal{E}}{\hbar w_x \cos\phi + s\hbar\sqrt{v_y^2 \sin^2\phi + v_x^2 \cos^2\phi}}. \tag{3.36}$$

q_y denotes the y component of the wave vector within the barrier and is given by

$$q_y = \frac{-1}{\hbar v_y}\sqrt{(\mathcal{E} - V_0 - \hbar(k_x + \mu\delta)w_x)^2 - \hbar^2 v_x^2 (k_x + \mu\delta)^2}. \tag{3.37}$$

Conservation of the transverse wave vector k_x and boundary conditions obtained by the continuity of the wave functions at the barrier interfaces give the transmission coefficient t

$$t = \frac{2e^{-ik_y L} s's \sin\theta_v \sin\phi_v}{s's(e^{iq_y L}\cos(\theta_v - \phi_v) - e^{-iq_y L}\cos(\theta_v + \phi_v)) - 2i \sin q_y L}. \tag{3.38}$$

Under resonance condition:

$$\frac{1}{\hbar v_y}\sqrt{(\mathcal{E}-V_0-\hbar(k_x+\delta)w_x)^2-\hbar^2 v_x^2(k_x+\delta)^2}=\frac{n\pi}{L}, n=0,\pm1,\pm2,\dots$$

the transmission amplitude (3.38) becomes $t = (-1)^n e^{-ik_yL}$, which corresponds to perfect transmission, i.e. $T = |t|^2 = 1$. It is shown in Figure 3.10 that the transmission probability T is not symmetric, contrary to that of fermions in graphene (2.11), with respect to normal incidence because of the anisotropy of Fermi velocity v_F. As it can be seen in Figure 2.2, Figure 2.7, and Figure 2.8, transmission profiles are symmetric with respect to the incident angle $\phi = \pi/2$, and $\theta = 0$ for the last two figures. It can be inferred that the presence of electrical barrier on the central region does not cause asymmetric transmission profiles in the case of graphene and non-tilted WSs. However, we have seen in Figure 2.12 that in the presence of magnetic field effect this symmetry is broken. Moreover, if the energy dispersion is tilted along one of the transverse directions, the transmission profiles are no longer symmetric with respect to the normal incidence as can be seen in Figures 2.9, 2.10, and 3.10(a,b,c). These examples show that one may obtain asymmetric transmission profiles in the presence of tilt parameter without magnetic field effect. Figure 3.10 is obtained under the approximations $v_x = v_y \approx 10^5$ ms^{-1}, $w_x \approx -0.8 \times 10^5$ and $w_y \approx 0$. The examples (a), (d), (e), and (f) demonstrate the angular dependence of transmission probability under the case of applied potential $V_0 = 3\mathcal{E}_F/4$. For plots (b), (g), (h), and (i) the potential height is $V_0 = 3\mathcal{E}_F/2$ and lastly, for the plot (c) $V_0 = 2\mathcal{E}_F$. The blue plots are obtained under the magnetic field strength (d) $B_z = 0.5$, (e) $B_z = 1.0$ and (f) $B_z = 3$ T while green ones are obtained in the case of (g) $B_z = -0.5$, (h) $B_z = -1$, and, lastly, (i) $B_z = -3$ T. Besides, it could be deduced that allowed transmission angle range increases as the height of the barrier increases. This can be understood by considering the overlap of the Fermi surfaces at the barrier interface which is shown in Figure 3.9. We consider the case without magnetic field effect. The constant energy curves (3.32) are ellipses. The shaded regions show the allowed range of the incident vectors for non-zero transmission. If the particle approaches the barrier with an angle which fall within the non-shaded range, it is totally reflected by the barrier.

This is because this angle range leads to imaginary q_y (3.37). Moreover, when the applied potential is close to the Fermi energy $\mathcal{E}_F$ the barrier becomes transparent only for the electrons approaching the square barrier at angles close to normal incidence. Small changes in incident angles may correspond to a noticeable change in transmission probability. As the magnetic field strength increases transmission profiles are shifted along the direction of the tilt as can be seen in Figure 3.10(d,e,f).

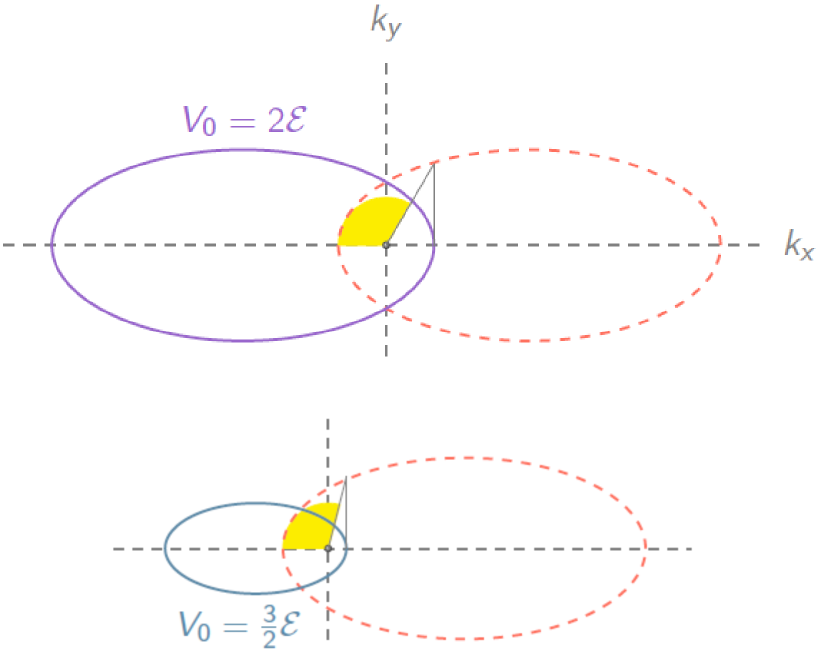

Figure 3.9. The Fermi surfaces of low-energy quasiparticles belong to different regions shown in Figure 3.7. The straight (dashed) curves represent the Fermi surfaces of quasiparticles in the absence (presence) of electric potential (top)$V_0 = 2\mathcal{E}_F$ and (bottom)$V_0 = \frac{3}{2}\mathcal{E}_F$ where $\mathcal{E}_F = 25$ meV.

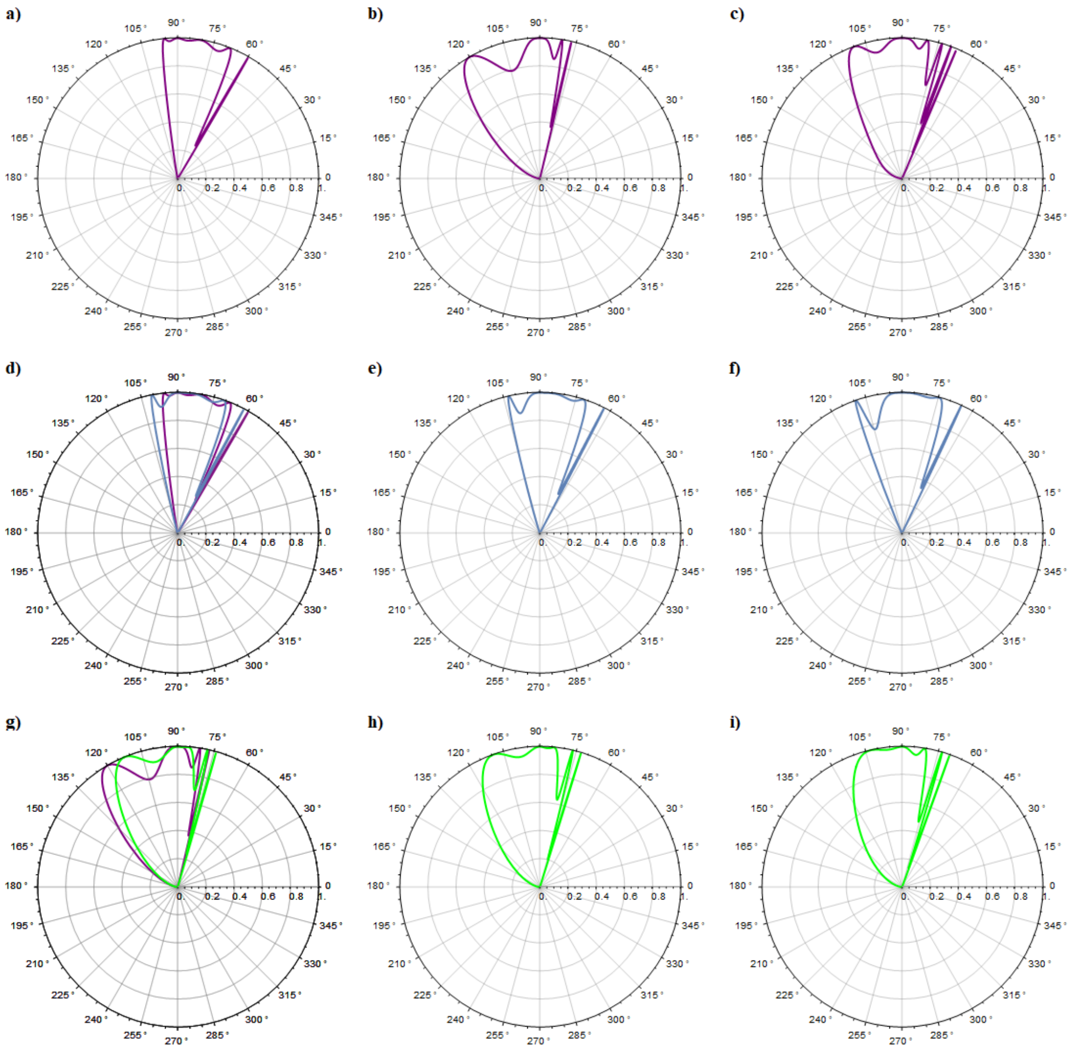

Figure 3.10. Polar plot of the transmission probability $T(\phi)$ for different configurations of applied potential. Fermi energy is 25 meV and the barrier width is chosen to be $L = 50$ nm.

4. CONCLUSION

Up to now, Klein tunnelling has been investigated in graphene in many aspects. Realization of Klein's gedanken experiment in 3D has, also, been made possible by discovery of Weyl semimetal. Recently, it has been shown that the low-energy quasiparticles present in quasi-2D organic compond α-(BEDT-TTF)$_2$I$_3$ obey the Weyl equation. We investigated the angular dependence of the transmission in this quasi-2D organic compound with or without magnetic field effect. The square-shaped potential barrier which has been used in our calculations may be obtained in Dirac and Weyl semimetals via alkaline metal doping or applying gate-voltage. However, Klein-like tunnelling in this quasi-2D organic compound has not been observed experimentally yet. Experimental control of the Fermi level by applying gate voltage is difficult due to the layered structure of this organic compound. Besides, alkaline metal doping has been shown to work well for inorganic systems. However, a recently published paper [52] proposes an efficient alkali metal doping system for organic crystals. Our results show that even without magnetic field effect the transmission profile is shifted due to the presence of a term which tilts the energy dispersion in this Weyl semimetal. Magnetic field effect, also, shifts the perfect transmission angles. When the applied potential is close to the Fermi energy $\mathcal{E}_F$ the barrier becomes transparent only for the electrons approaching the square barrier at angles close to the normal incidence. Besides, the perfect transmission angle range increases with increasing potential barrier height.

REFERENCES

1. Katsnelson, M., K. Novoselov and A. Geim, “Chiral tunnelling and the Klein paradox in graphene”, *Nature physics*, Vol. 2, No. 9, p. 620, 2006.

2. Yesilyurt, C., S. G. Tan, G. Liang *et al.*, “Klein tunneling in Weyl semimetals under the influence of magnetic field”, *Scientific reports*, Vol. 6, p. 38862, 2016.

3. Soluyanov, A. A., D. Gresch, Z. Wang *et al.*, “Type-ii weyl semimetals”, *Nature*, Vol. 527, No. 7579, p. 495, 2015.

4. Tajima, N. and K. Kajita, “Experimental study of organic zero-gap conductor α-(BEDT-TTF)$_2$I$_3$”, *Science and Technology of Advanced Materials*, Vol. 10, No. 2, p. 024308, 2009, `http://stacks.iop.org/1468-6996/10/i=2/a=024308`.

5. Kobayashi, A., S. Katayama and Y. Suzumura, “Theoretical study of the zero-gap organic conductor α-(BEDT-TTF)$_2$I$_3$”, *Science and Technology of Advanced Materials*, Vol. 10, No. 2, p. 024309, 2009, `http://stacks.iop.org/1468-6996/10/i=2/a=024309`.

6. Katayama, S., Kobayashi, A. and Suzumura, Y., “Electronic properties close to Dirac cone in two-dimensional organic conductor α-(BEDT-TTF)$_2$I$_3$”, *Eur. Phys. J. B*, Vol. 67, No. 2, pp. 139–148, 2009, `https://doi.org/10.1140/epjb/e2009-00020-0`.

7. Cayssol, J., “Introduction to Dirac materials and topological insulators”, *Comptes Rendus Physique*, Vol. 14, pp. 760–778, Nov. 2013.

8. Goerbig, M. O., “Electronic properties of graphene in a strong magnetic field”, *Rev. Mod. Phys.*, Vol. 83, pp. 1193–1243, Nov 2011, `https://link.aps.org/doi/10.1103/RevModPhys.83.1193`.

9. Kino, H. and T. Miyazaki, “First-Principles Study of Electronic Structure in α-(BEDT-TTF)$_2$I$_3$ at Ambient Pressure and with Uniaxial Strain”, *Journal of the Physical Society of Japan*, Vol. 75, No. 3, p. 034704, 2006, `https://doi.org/10.1143/JPSJ.75.034704`.

10. Burkov, A., “Topological semimetals”, *Nature materials*, Vol. 15, No. 11, p. 1145, 2016.

11. Trescher, M., B. Sbierski, P. W. Brouwer *et al.*, “Tilted disordered Weyl semimetals”, *Physical Review B*, Vol. 95, No. 4, p. 045139, 2017.

12. Wehling, T., A. Black-Schaffer and A. Balatsky, “Dirac materials”, *Advances in Physics*, Vol. 63, No. 1, pp. 1–76, 2014, `https://doi.org/10.1080/00018732.2014.927109`.

13. Liu, Z., J. , B. Zhou *et al.*, “A stable three-dimensional topological Dirac semimetal Cd$_3$As$_2$”, *Nature materials*, Vol. 13, No. 7, p. 677, 2014.

14. Xu, N., H. Weng, B. Lv *et al.*, “Observation of Weyl nodes and Fermi arcs in tantalum phosphide”, *Nature communications*, Vol. 7, p. 11006, 2016.

15. Nielsen, H. and M. Ninomiya, “Absence of neutrinos on a lattice: (I). Proof by homotopy theory”, *Nuclear Physics B*, Vol. 185, No. 1, pp. 20 – 40, 1981, `http://www.sciencedirect.com/science/article/pii/0550321381903618`.

16. Nielsen, H. and M. Ninomiya, “A no-go theorem for regularizing chiral fermions”, *Physics Letters B*, Vol. 105, No. 2, pp. 219 – 223, 1981, `http://www.sciencedirect.com/science/article/pii/0370269381910261`.

17. Klein, O., “Die Reflexion von Elektronen an einem Potentialsprung nach der relativistischen Dynamik von Dirac”, *Zeitschrift für Physik*, Vol. 53, No. 3-4, pp. 157–165, 1929.

18. Tudorovskiy, T., K. J. A. Reijnders and M. I. Katsnelson, “Chiral tunneling in single-layer and bilayer graphene”, *Physica Scripta*, Vol. 2012, No. T146, p. 014010, 2012, `http://stacks.iop.org/1402-4896/2012/i=T146/a=014010`.

19. Casanova, J., J. J. García-Ripoll, R. Gerritsma *et al.*, “Klein tunneling and Dirac potentials in trapped ions”, *Phys. Rev. A*, Vol. 82, p. 020101, Aug 2010, `https://link.aps.org/doi/10.1103/PhysRevA.82.020101`.

20. Salger, T., C. Grossert, S. Kling *et al.*, “Klein Tunneling of a Quasirelativistic Bose-Einstein Condensate in an Optical Lattice”, *Phys. Rev. Lett.*, Vol. 107, p. 240401, Dec 2011, `https://link.aps.org/doi/10.1103/PhysRevLett.107.240401`.

21. Bala Kumar, S., M. B. A. Jalil and S. G. Tan, “Klein tunneling in graphene systems under the influence of magnetic field”, *Journal of Applied Physics*, Vol. 114, No. 8, p. 084314, 2013, `https://doi.org/10.1063/1.4819799`.

22. Lv, B. Q., H. M. Weng, B. B. Fu *et al.*, “Experimental Discovery of Weyl Semimetal TaAs”, *Phys. Rev. X*, Vol. 5, p. 031013, Jul 2015, `https://link.aps.org/doi/10.1103/PhysRevX.5.031013`.

23. Lv, B., N. Xu, H. Weng *et al.*, “Observation of Weyl nodes in TaAs”, *Nature Physics*, Vol. 11, No. 9, p. 724, 2015.

24. Xu, S.-Y., N. Alidoust, I. Belopolski *et al.*, “Discovery of a Weyl fermion state with Fermi arcs in niobium arsenide”, *Nature Physics*, Vol. 11, No. 9, p. 748, 2015.

25. Yesilyurt, C., Z. B. Siu, S. G. Tan *et al.*, “Anomalous tunneling characteristic of Weyl semimetals with tilted energy dispersion”, *Applied Physics Letters*, Vol. 111, No. 6, p. 063101, 2017, `https://doi.org/10.1063/1.4997296`.

26. Sakurai, J. J., *Advanced quantum mechanics*, Pearson Education India, 1967.

27. Calogeracos, A. and N. Dombey, “History and physics of the Klein

paradox", *Contemporary Physics*, Vol. 40, No. 5, pp. 313–321, 1999, `https://doi.org/10.1080/001075199181387`.

28. Sauter, F., "Über das Verhalten eines Elektrons im homogenen elektrischen Feld nach der relativistischen Theorie Diracs", *Zeitschrift für Physik*, Vol. 69, No. 11, pp. 742–764, Nov 1931, `https://doi.org/10.1007/BF01339461`.

29. Hund, F., "Materieerzeugung im anschaulichen und im gequantelten Wellenbild der Materie", *Zeitschrift für Physik*, Vol. 117, No. 1, pp. 1–17, Jan 1941, `https://doi.org/10.1007/BF01337403`.

30. Castro Neto, A. H., F. Guinea, N. M. R. Peres *et al.*, "The electronic properties of graphene", *Rev. Mod. Phys.*, Vol. 81, pp. 109–162, Jan 2009, `https://link.aps.org/doi/10.1103/RevModPhys.81.109`.

31. Novoselov, K. S., A. K. Geim, S. V. Morozov *et al.*, "Electric Field Effect in Atomically Thin Carbon Films", *Science*, Vol. 306, No. 5696, pp. 666–669, 2004, `http://science.sciencemag.org/content/306/5696/666`.

32. Novoselov, K. S., A. K. Geim, S. Morozov *et al.*, "Two-dimensional gas of massless Dirac fermions in graphene", *nature*, Vol. 438, No. 7065, p. 197, 2005.

33. Geim, A. K. and K. S. Novoselov, "The rise of graphene", *Nanoscience and Technology: A Collection of Reviews from Nature Journals*, pp. 11–19, World Scientific, 2010.

34. Zhang, Y., Y.-W. Tan, H. L. Stormer *et al.*, "Experimental observation of the quantum Hall effect and Berry's phase in graphene", *nature*, Vol. 438, No. 7065, p. 201, 2005.

35. Nogaret, A., S. J. Bending and M. Henini, "Resistance Resonance Effects through Magnetic Edge States", *Phys. Rev. Lett.*, Vol. 84, pp. 2231–2234, Mar 2000, `https://link.aps.org/doi/10.1103/PhysRevLett.84.2231`.

36. Papp, G. and F. M. Peeters, “Spin filtering in a magnetic–electric barrier structure”, *Applied Physics Letters*, Vol. 78, No. 15, pp. 2184–2186, 2001, `https://doi.org/10.1063/1.1360224`.

37. Xu, S.-Y., I. Belopolski, N. Alidoust *et al.*, “Discovery of a Weyl fermion semimetal and topological Fermi arcs”, *Science*, Vol. 349, No. 6248, pp. 613–617, 2015, `http://science.sciencemag.org/content/349/6248/613`.

38. Liu, Z., L. Yang, Y. Sun *et al.*, “Evolution of the Fermi surface of Weyl semimetals in the transition metal pnictide family”, *Nature materials*, Vol. 15, No. 1, p. 27, 2016.

39. Sun, Y., S.-C. Wu, M. N. Ali *et al.*, “Prediction of Weyl semimetal in orthorhombic $MoTe_2$”, *Phys. Rev. B*, Vol. 92, p. 161107, Oct 2015, `https://link.aps.org/doi/10.1103/PhysRevB.92.161107`.

40. Chang, T.-R., S.-Y. Xu, G. Chang *et al.*, “Prediction of an arc-tunable Weyl Fermion metallic state in $Mo_xW_{1-x}Te_2$”, *Nature communications*, Vol. 7, p. 10639, 2016.

41. Jiang, J., Z. Liu, Y. Sun *et al.*, “Signature of type-II Weyl semimetal phase in $MoTe_2$”, *Nature communications*, Vol. 8, p. 13973, 2017.

42. Liu, Y., C. Zhang, X. Yuan *et al.*, “Gate-tunable quantum oscillations in ambipolar Cd_3As_2 thin films”, *NPG Asia Materials*, Vol. 7, No. 10, p. e221, 2015.

43. Wang, Y., E. Liu, H. Liu *et al.*, “Gate-tunable negative longitudinal magnetoresistance in the predicted type-II Weyl semimetal WTe_2”, *Nature communications*, Vol. 7, p. 13142, 2016.

44. Bai, C., Y. Yang and K. Chang, “Chiral tunneling in gated inversion symmetric Weyl semimetal”, *Scientific reports*, Vol. 6, p. 21283, 2016.

45. Jr, J. M. P., F. M. Peeters, A. Chaves *et al.*, "Klein tunneling in single and multiple barriers in graphene", *Semiconductor Science and Technology*, Vol. 25, No. 3, p. 033002, 2010, `http://stacks.iop.org/0268-1242/25/i=3/a=033002`.

46. Singleton, J., *Band Theory and Electronic Properties of Solids*, Oxford Master Series in Condensed Matter Physics, OUP Oxford, 2001, `https://books.google.com.tr/books?id=8vVBkvZLzrIC`.

47. Katayama, S., A. Kobayashi and Y. Suzumura, "Pressure-Induced Zero-Gap Semiconducting State in Organic Conductor α-(BEDT-TTF)$_2$I$_3$ Salt", *Journal of the Physical Society of Japan*, Vol. 75, No. 5, p. 054705, 2006, `https://doi.org/10.1143/JPSJ.75.054705`.

48. Kajita, K., Y. Nishio, N. Tajima *et al.*, "Molecular Dirac Fermion Systems — Theoretical and Experimental Approaches —", *Journal of the Physical Society of Japan*, Vol. 83, p. 072002, 07 2014.

49. Hirata, M., K. Ishikawa, K. Miyagawa *et al.*, "Observation of an anisotropic Dirac cone reshaping and ferrimagnetic spin polarization in an organic conductor", *Nature communications*, Vol. 7, p. 12666, 2016.

50. Kobayashi, A., S. Katayama, Y. Suzumura *et al.*, "Massless Fermions in Organic Conductor", *Journal of the Physical Society of Japan*, Vol. 76, No. 3, p. 034711, 2007, `https://doi.org/10.1143/JPSJ.76.034711`.

51. Goerbig, M. O., J.-N. Fuchs, G. Montambaux *et al.*, "Tilted anisotropic Dirac cones in quinoid-type graphene and α-(BEDT-TTF)$_2$I$_3$", *Phys. Rev. B*, Vol. 78, p. 045415, Jul 2008, `https://link.aps.org/doi/10.1103/PhysRevB.78.045415`.

52. Lee, J., C. Park, I. Song *et al.*, "Highly reproducible alkali metal doping system for organic crystals through enhanced diffusion of alkali metal by secondary thermal activation", *Scientific reports*, Vol. 8, No. 1, p. 7617, 2018.

53. Datta, S., *Quantum Transport: Atom to Transistor*, Cambridge University Press, 2005.

54. Russo, S., M. F. Craciun, T. Khodkov *et al.*, “Electronic Transport Properties of Few-Layer Graphene Materials”, J. R. Gong (Editor), *Graphene*, chap. 9, IntechOpen, Rijeka, 2011, `https://doi.org/10.5772/22530`.

APPENDIX A: GRAPHENE

A.1. Hexagonal Lattice Structure

Graphene is a 2D material build up carbon atoms arranged in hexagonal, honeycomb, pattern as shown in Figure A.1. If we consider a unit cell consisting one carbon atom, then it can be seen that this pattern is not periodic. In the perspective of green coloured atom, there are three nearest neighbours in the directions south, north-west, and north-east while any white coloured atom has nearest neighbours in north, south-east, and south-west directions. So, atoms in unit cells do not have identical environments. If, however, one consider a unit cell formed by two carbon atoms A and B as shown in Figure A.1, the obtained structure satisfies the periodicity.

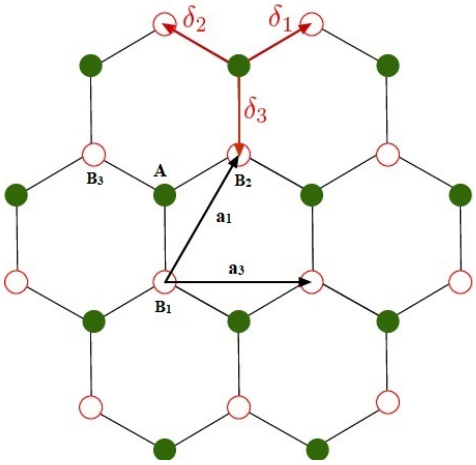

Figure A.1. Graphene honeycomb lattice structure. $\mathrm{B}_1, \mathrm{B}_2$, and B_3 are nearest-neighbour sites of the atom A. The vectors $\boldsymbol{\delta_i}$s, where $i = 1, 2, 3$, connect a given site to its nearest-neighbours. Figure from Reference [7].

The lattice vectors spanning this 2D triangular Bravais lattice can be written as

$$\mathbf{a_1} = \frac{\sqrt{3}a_0}{2}\hat{x} + \frac{3a_0}{2}\hat{y} \quad \text{and} \quad \mathbf{a_2} = \frac{-\sqrt{3}a_0}{2}\hat{x} + \frac{3a_0}{2}\hat{y} \tag{A.1}$$

where a_0 is the spacing between two adjacent carbon atoms A and B and is given by $a_0 \approx 1.42$ Å. Every point on this lattice structure can be described by a set of integers (m, n) where the lattice translation vector $\mathbf{R} = m\mathbf{a_1} + n\mathbf{a_2}$. The three nearest neighbour vectors in real space are following:

$$\gamma_\mathbf{1} = \frac{\sqrt{3}a_0}{2}\hat{x} + \frac{a_0}{2}\hat{y}, \quad \gamma_\mathbf{2} = -\frac{\sqrt{3}a_0}{2}\hat{x} + \frac{a_0}{2}\hat{y}, \quad \text{and} \quad \gamma_\mathbf{3} = -a_0\hat{y} \tag{A.2}$$

The basis vectors for the reciprocal lattice are obtained by Fourier transforming the lattice vectors (A.1) and are given by

$$\mathbf{b_1} = \frac{2\pi(\mathbf{a_2} \times \hat{z})}{\mathbf{a_1} \cdot (\mathbf{a_2} \times \hat{z})} = \frac{2\pi}{\sqrt{3}a_0}(1, \frac{1}{\sqrt{3}}), \quad \mathbf{b_2} = \frac{2\pi(\hat{z} \times \mathbf{a_1})}{\mathbf{a_2} \cdot (\hat{z} \times \mathbf{a_1})} = \frac{2\pi}{\sqrt{3}a_0}(-1, \frac{1}{\sqrt{3}}). \tag{A.3}$$

The first Brillouin zone is constructed by drawing perpendicular bisectors of the lines joining the origin to the neighbours in the reciprocal lattice and gives the allowed values of $\mathbf{k}$ [53]. Two corners of the BZ are of particular importance and are given by

$$\mathbf{K} = \frac{4\pi}{3\sqrt{3}a_0}\hat{k_x}, \quad \mathbf{K}' = -\frac{4\pi}{3\sqrt{3}a_0}\hat{k_x} \tag{A.4}$$

in momentum space. These are called Dirac points. The remaining corners can be connected to the Dirac points by means of a translation by a reciprocal lattice vector $\mathbf{T} = m\mathbf{b_1} + n\mathbf{b_2}$, where $m, n = 0, \pm 1, \pm 2, \ldots$. It is important to note that the inequivalence between these points have nothing to do with inequivalent carbon atoms placed in a single unit cell. The first BZ is formed by Bravais lattice in real space irrespective of the number of atoms in the unit cell [8].

On a side note we briefly examine the hybridization of carbon atoms in honeycomb lattice.

Carbon atom ^{12}C has 6 electrons being in configuration $1s^2 2s^2 2p^2$ in atomic ground state as can be seen in Figure A.2. In the presence of other carbon atoms, excitation of one electron from $2s$ orbital to $2p_z$ orbital is favorable so that the atom can form covalent bonds with neighbouring carbon atoms. In the excited state the quantum-mechanical states $|2s\rangle$ mixes with $n|2p_i\rangle$ state to construct a sp^n hybridization. In graphene case the superposition of the state $|2s\rangle$ with $|2p_x\rangle$ and $|2p_y\rangle$ states leads to planar sp^2 hybridization and overlapping sp^2 orbitals of two adjacent carbon atoms, therefore, form a covalent σ-bond. Each angle between three sp^2 orbitals is 120°. Then overlapping the remaining $2p_z$ orbitals which are perpendicular to the plane form a covalent π-bond which is weaker than the former. In the hexagonal lattice structure the π electrons, i.e. electrons in π-bonds, are responsible for the low-energy excitation [54].

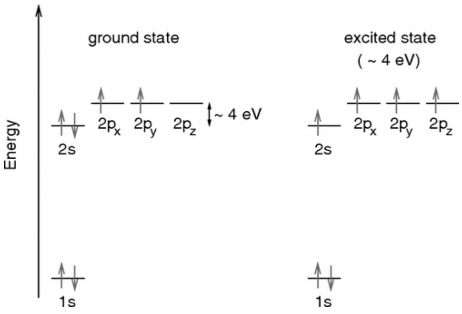

Figure A.2. Electronic configuration for carbon atom in the ground and excited state. Figure from Reference [8].

A.2. The Low-Energy Excitations of π Electrons

The electronic energy dispersion relation of graphene is, in general, obtained using the tight-binding method with nearest-neighbour (nn) tranfer energy t and next-nearest-neighbour (nnn) hopping amplitude t'.

This results

$$\begin{aligned}\mathcal{E}_{\mathbf{k}}^{\xi} &\approx (t' - st)|\gamma_{\mathbf{k}}|^2 + \xi t|\gamma_{\mathbf{k}}| \\ &= 2(t' - st)\sum_{i=1}^{3}\cos(\mathbf{k}\cdot\mathbf{a}_i) + \xi t\sqrt{2\sum_{i=1}^{3}\cos(\mathbf{k}\cdot\mathbf{a}_i) + 3}\end{aligned} \tag{A.5}$$

where $t' - st = -0.3$ eV, $\xi = \pm 1$, and $\gamma_{\mathbf{k}} = 1 + e^{-i\mathbf{k}\cdot\mathbf{a}_1} + e^{-i\mathbf{k}\cdot\mathbf{a}_2}$. The energy dispersion can be seen in Figure A.3.

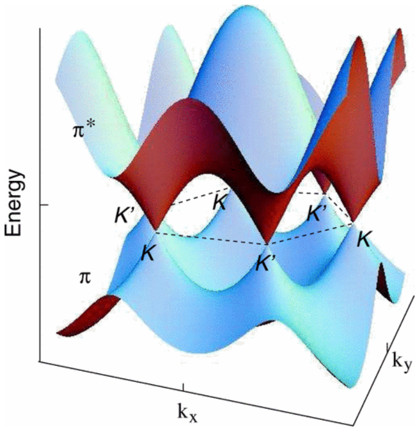

Figure A.3. Energy dispersion obtained within the tight-binding method. Figure from Reference [8].

The upper and lower bands are called conduction and valence bands which are denoted by the index $\xi = \pm$, respectively. As we stated each carbon atom contributes one π electron and it occupies either spin-up or spin-down state. For this reason, while the valence band is completely filled, the conduction band is absolutely empty. As shown in Figure A.3, the cosine-like energy bands coincide at the points **K** and **K′** in the first BZ and the Fermi level is placed at these points. These are called Dirac points for reasons which are clarified later in this subsection. Dirac points can be obtained by setting $\gamma_{\mathbf{k}} = 0$, i.e.

$$\gamma_{\mathbf{k}} = 1 + e^{-i\mathbf{k}^D\cdot\mathbf{a}_1} + e^{-i\mathbf{k}^D\cdot\mathbf{a}_2} = 0.$$

This equality is satisfied when

$$\mathrm{Re}(\gamma_{\mathbf{k}}) = 1 + \cos\left(\frac{\sqrt{3}a_0}{2}k_x^D + \frac{3a_0}{2}k_y^D\right) + \cos\left(-\frac{\sqrt{3}a_0}{2}k_x^D + \frac{3a_0}{2}k_y^D\right) = 0 \tag{A.6}$$

and

$$\mathrm{Im}(\gamma_{\mathbf{k}}) = \sin\left(\frac{\sqrt{3}a_0}{2}k_x^D + \frac{3a_0}{2}k_y^D\right) + \sin\left(-\frac{\sqrt{3}a_0}{2}k_x^D + \frac{3a_0}{2}k_y^D\right) = 0. \tag{A.7}$$

With the choice of

$$k_x^D = \pm\frac{4\pi}{3\sqrt{3}a_0} \quad \text{and} \quad k_y^D = 0$$

one can, therefore, obtain two Dirac points

$$\mathbf{K} = \frac{4\pi}{3\sqrt{3}a_0}\hat{k}_x \quad \text{and} \quad \mathbf{K}' = -\frac{4\pi}{3\sqrt{3}a_0}\hat{k}_x. \tag{A.8}$$

Notice that each corners of the first BZ satisfy Equations A.6 and A.7 and they can be put into two groups

$$\begin{aligned}(k_x, k_y) &= \left(\frac{4\pi}{3\sqrt{3}a_0}, 0\right), -\frac{2\pi}{3a_0}\left(\frac{1}{\sqrt{3}}, -1\right), -\frac{2\pi}{3a_0}\left(\frac{1}{\sqrt{3}}, 1\right) \\ (k_x, k_y) &= -\left(\frac{4\pi}{3\sqrt{3}a_0}, 0\right), \frac{2\pi}{3a_0}\left(\frac{1}{\sqrt{3}}, 1\right), \frac{2\pi}{3a_0}\left(\frac{1}{\sqrt{3}}, -1\right).\end{aligned} \tag{A.9}$$

The points within the same group can be considered as crystallographically equivalent since they can be connected to one of the Dirac points by a reciprocal lattice vector. Hence, there said to be only two inequivalent Dirac points, namely **K** and **K′**. Furthermore, each corner of the first BZ has one-third of a valley around it within the zone and it can be thought that there are two full valleys within the BZ around the points **K** and **K′** since the parts of the valleys can be translated by appropriate lattice vectors [53] as mentioned above.

Moreover, due to time-reversal symmetry resulting in an equality $\mathcal{E}_{\mathbf{k}} = \mathcal{E}_{-\mathbf{k}}$ which can be seen from Equation A.5 the Fermi energy is said to be doubly degenerate. That is to say if $\mathbf{k}^D$ is a point at which two bands touch each other, then $-\mathbf{k}^D$ must be the other point at which conduction and valence bands coincide the Fermi energy.

A.2.1. Effective Tight-Binding Hamiltonian

Before examining the low-energy excitations, we can define an effective tight-binding Hamiltonian by taking into consideration only nn and nnn hopping amplitudes

$$\mathcal{H}_{\mathbf{k},\text{eff}} \equiv t'|\gamma_{\mathbf{k}}|^2 \mathbb{I} + t \begin{bmatrix} 0 & \gamma_{\mathbf{k}} \\ \gamma^*_{\mathbf{k}} & 0 \end{bmatrix}. \tag{A.10}$$

So as to consider the low-energy excitations, that is to say the electronic excitations of which characteristic energy $\mathcal{E}_{\mathbf{k}}$ is much smaller than the absolute value of nn hopping amplitude $\mathcal{E}_{\mathbf{k}} \ll |t|$, one may expand $\gamma_{\mathbf{k}}$ around the Dirac points $\mathbf{K}^{(')}$ to the first order in $|\tilde{\mathbf{k}}| \equiv |\mathbf{k} \mp \mathbf{K}|$

$$\begin{aligned}
\gamma^*_{\mathbf{k}} &= 1 + e^{i\mathbf{k}\cdot\mathbf{a}_1} + e^{i\mathbf{k}\cdot\mathbf{a}_2} \\
&= 1 + e^{\pm i\mathbf{K}\cdot\mathbf{a}_1} e^{i\tilde{\mathbf{k}}\cdot\mathbf{a}_1} + e^{\pm i\mathbf{K}\cdot\mathbf{a}_2} e^{i\tilde{\mathbf{k}}\cdot\mathbf{a}_2} \\
&\simeq 1 + e^{\pm i\frac{2\pi}{3}}(1 + i\tilde{\mathbf{k}}\cdot\mathbf{a}_1) + e^{\mp i\frac{2\pi}{3}}(1 + i\tilde{\mathbf{k}}\cdot\mathbf{a}_2) \\
&= i(e^{\pm i\frac{2\pi}{3}}\tilde{\mathbf{k}}\cdot\mathbf{a}_1 + e^{\mp i\frac{2\pi}{3}}\tilde{\mathbf{k}}\cdot\mathbf{a}_2) \\
&= i\frac{\sqrt{3}a_0}{2}\left[(\tilde{k}_x + \sqrt{3}\tilde{k}_y)e^{\pm i\frac{2\pi}{3}} + (-\tilde{k}_x + \sqrt{3}\tilde{k}_y)e^{\mp i\frac{2\pi}{3}}\right] \\
&= \mp\frac{3a_0}{2}(\tilde{k}_x \pm i\tilde{k}_y)
\end{aligned} \tag{A.11}$$

where we have assumed $|\tilde{\mathbf{k}}|a_0 \ll 1$. We do not take into account the term t' since it is proportional to $|\gamma_{\mathbf{k}}|^2$ which contributes the low-energy Hamiltonian at the order of $|\tilde{\mathbf{k}}|^2 a_0^2$.

Thus the effective Hamiltonian around the Dirac points ±**K** reads

$$\mathcal{H}_{\tilde{\mathbf{k}},\text{eff}} = \mp\hbar\frac{3a_0}{2}t\begin{bmatrix} 0 & \tilde{k}_x \mp i\tilde{k}_y \\ \tilde{k}_x \pm i\tilde{k}_y & 0 \end{bmatrix} \tag{A.12}$$

or equivalently,

$$\mathcal{H}_{\tilde{\mathbf{k}},\text{eff}} = \mp i\hbar v_F(\boldsymbol{\sigma}^{(\prime)}\cdot\boldsymbol{\nabla}) \tag{A.13}$$

where $\boldsymbol{\sigma} = (\sigma_x, \sigma_y)$ and $\boldsymbol{\sigma}' = (\sigma_x, -\sigma_y)$ for the points **K** and **K**′, respectively.The Fermi velocity v_F has been defined by $v_F \equiv -\frac{3a_0}{2}t \approx 10^6$ ms^{-1} which plays a similar role in graphene as the speed of light. Since the nearest-neighbour hopping parameter $t \approx -3$ eV is negative as stated previously the minus sign renders the Fermi velocity positive. Note that the factor ∓ 1 in Equation A.13 defines the valley isospin, where -1 represents the point **K** and +1 represents the other Dirac point **K**′. The energy eigenvalues of the effective Hamiltonian (A.13) are given by

$$\mathcal{E}_{\tilde{\mathbf{k}}} = \xi\hbar v_F|\tilde{\mathbf{k}}|, \quad \xi = \pm \tag{A.14}$$

As mentioned above the requirement $\mathcal{E}_{\mathbf{k}} \ll |t|$ is provided by the continuum limit $|\tilde{\mathbf{k}}|a_0 \ll 1$ since

$$|\mathcal{E}_{\tilde{\mathbf{k}}}| = \frac{3}{2}\hbar|t||\tilde{\mathbf{k}}|a_0 \ll |t|.$$

It may be remarked that the energy dispersion relation (A.14) is independent of the valley isospin λ. Thus, it can be stated the twofold valley degeneracy met at the level of Fermi energy exists when regarding the low-energy excitations around the Dirac points.

Close to the point $\mathbf{K}$, the two-component wave function $\psi_{\mathbf{k}}(\mathbf{r})$ obeys the 2D Dirac equation

$$-i\hbar v_F \boldsymbol{\sigma} \cdot \nabla \psi_{\mathbf{k}}(\mathbf{r}) = \mathcal{E}_\xi \psi_{\mathbf{k}}(\mathbf{r}). \tag{A.15}$$

Therefore, the wave function in momentum space around the point $\mathbf{K}$ is

$$\psi_{\mathbf{K}} = \frac{1}{\sqrt{2}} \begin{pmatrix} 1 \\ \xi e^{i\phi} \end{pmatrix} \tag{A.16}$$

where we have defined $\phi \equiv \arctan\left(\frac{k_y}{k_x}\right)$. Besides, with the help of the equation

$$i\hbar v_F \boldsymbol{\sigma'} \cdot \nabla \psi_{\mathbf{k}}(\mathbf{r}) = \mathcal{E}_\xi \psi_{\mathbf{k}}(\mathbf{r}) \tag{A.17}$$

derived from Equation A.13, one can obtain the wave function around $\mathbf{K}'$

$$\psi_{\mathbf{K}'} = \frac{1}{\sqrt{2}} \begin{pmatrix} 1 \\ -\xi e^{-i\phi} \end{pmatrix}. \tag{A.18}$$

The top and bottom components of the electron wave function $\psi_{\mathbf{K}}$ represent A and B sublattices at the point $\mathbf{K}$, respectively and they can be interpreted as the probability amplitudes of the Bloch wave function

$$\psi_{\mathbf{k}}(\mathbf{r}) = a_{\mathbf{k}} \psi_{\mathbf{k}}^{A}(\mathbf{r}) + b_{\mathbf{k}} \psi_{\mathbf{k}}^{B}(\mathbf{r}) \tag{A.19}$$

on the sublattices A and B. Hence, it can be deduced that the probabilities to find an electron in the state $\psi_{\mathbf{K}}$ on the sublattices A and B are equal due to the fact that both sublattices are constructed from carbon atoms with the same on-site energy.

A.2.1.1. Chirality. Helicity of a particle is defined as the projection of its spin onto the direction of propagation

$$\eta_{\mathbf{k}} = \frac{\mathbf{k} \cdot \boldsymbol{\sigma}}{|\mathbf{k}|} \tag{A.20}$$

where $\boldsymbol{\sigma}$ represents the physical spin of the particle [8]. It is a unitary and Hermitian operator with the eigenvalues $\eta = \pm 1$. Since $\eta_{\mathbf{k}}$ commutes with Dirac Hamiltonian (A.13) describing massless Dirac fermions, helicity is considered as a good quantum number. One may separate the quantum state of a particle ψ into two components by means of the chiral projection operators, namely $P_+ = \frac{1+\eta_{\mathbf{k}}}{2}$ and $P_- = \frac{1-\eta_{\mathbf{k}}}{2}$,

$$\psi_L \equiv P_- \psi \quad \text{and} \quad \psi_R \equiv P_+ \psi. \tag{A.21}$$

For massless Dirac fermions one can find out the following relations:

$$\psi_L^- = \frac{1-\eta_{\mathbf{k}}}{2}\psi_- = \psi_-, \quad \psi_R^- = \frac{1+\eta_{\mathbf{k}}}{2}\psi_- = 0 \tag{A.22}$$

and

$$\psi_L^+ = \frac{1-\eta_{\mathbf{k}}}{2}\psi_+ = 0, \quad \psi_R^+ = \frac{1+\eta_{\mathbf{k}}}{2}\psi_+ = \psi_+. \tag{A.23}$$

Here, $\psi_\pm$ represents the eigenstates of the helicity operator corresponding the eigenvalues $\eta = \pm 1$. With the help of Equations A.22 and A.23 one may identify the notion of helicity and chirality for massless Dirac fermions close to Dirac points $\mathbf{K}$ and $\mathbf{K}'$.

The charge carriers in graphene are electrons and holes which can be seen as massless Dirac fermions. As stated before, the bands above and below the Fermi energy are called conduction and valence band, respectively. If the valence band is not fully occupied, then the allowed negative energy states behave as holes, positively charged particles while in the conduction band the current carrying states are electron-like.

If we consider the charge carriers in graphene, $\boldsymbol{\sigma}$ in Equation A.13 is interpreted as the pseudospin associated with the sublattices instead of physical spin. In this case, one can express the effective Hamiltonian (A.13) in terms of the helicity operator $\eta_{\mathbf{k}}$

$$\mathcal{H}_{\mathbf{k},\text{eff}} = \lambda \hbar v_F |\mathbf{k}| \eta_{\mathbf{k}} \tag{A.24}$$

where λ denotes the valley isospin, $\lambda = +1$ for the point $\mathbf{K}$ and $\lambda = -1$ for the other Dirac point $\mathbf{K}'$. As can be clearly seen from the last equation, helicity operator $\eta_{\mathbf{k}}$ commutes with 2D Dirac Hamiltonian $\mathcal{H}_{\mathbf{k},\text{eff}}$ for massless particles, i.e. $[\mathcal{H}_{\mathbf{k},\text{eff}}, \eta_{\mathbf{k}}] = 0$. This means that the states $\psi_{\mathbf{K}}$ and $\psi_{\mathbf{K}'}$ are also eigenstates of the helicity operator $\eta_{\mathbf{k}}$,

$$\frac{\mathbf{k}\cdot\boldsymbol{\sigma}}{|\mathbf{k}|}\psi_{\mathbf{K}} = \pm\psi_{\mathbf{K}} \quad \text{and} \quad \frac{\mathbf{k}\cdot\boldsymbol{\sigma'}}{|\mathbf{k}|}\psi_{\mathbf{K}'} = \mp\psi_{\mathbf{K}'}. \tag{A.25}$$

Additionally, the band index ξ is expressed by the valley pseudospin and chirality

$$\xi = \lambda\eta. \tag{A.26}$$

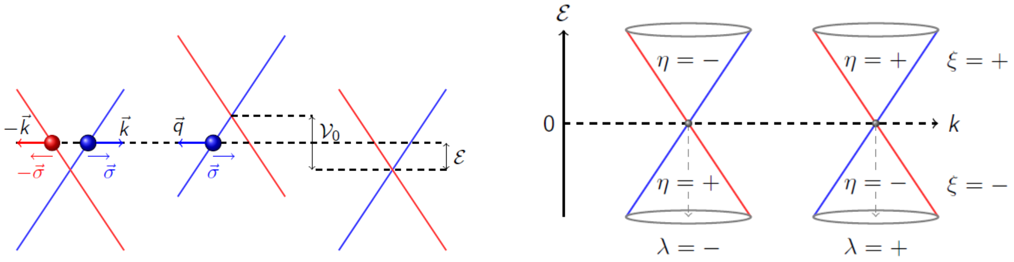

Figure A.4. Schematic diagrams of the spectrum of quasiparticles in graphene [1]. In the left plot it is shown that the pseudospin $\boldsymbol{\sigma}$ is parallel(antiparallel) to the direction of motion of the electrons(holes). The relation between band index ξ, valley spin λ, and chirality η in graphene is depicted in the right plot. Figure from Reference [8].

The last relation is illustrated in Figure A.4 (right plot). It can also be seen in Figure A.4 (left plot) that an electron moving to the right with positive energy originates from the same branch of the band diagram as hole propagating in the opposite direction with negative energy. These electron and hole states, thus, are said to be conjugated. The pseudospin $\boldsymbol{\sigma}$ of electrons and holes keeps a fixed direction along the same branch of the electronic spectrum which is parallel to the momentum for the former and anti-parallel for the latter.

APPENDIX B: CHIRALITY

We defined the Gamma matrices previously by using Sakurai's notation [26] in Chapter 2. However, the Gamma matrices can be expressed in Dirac representation or Weyl, chiral, representation. The latter choice of representation provides convenience with expressing the chiral projections as explained subsequently. According to the chiral representation the four contravariant gamma matrices, $\{\gamma^0, \gamma^1, \gamma^2, \gamma^3\}$, are

$$\gamma^0 = \begin{pmatrix} 0 & \mathbb{I} \\ \mathbb{I} & 0 \end{pmatrix}, \quad \gamma^k = \begin{pmatrix} 0 & \sigma^k \\ -\sigma^k & 0 \end{pmatrix}, \quad k = 1, 2, 3 \tag{B.1}$$

where σ^μ represent the Pauli spin matrices and $\mathbb{I}$ is the 2×2 identity matrix. The Gamma matrices in Weyl representation satisfy the following anticommutation relations:

$$\{\gamma^\mu, \gamma^\nu\} = 2\eta^{\mu\nu}\mathbb{I}_4, \quad \mu, \nu = 0, 1, 2, 3 \tag{B.2}$$

where $\eta^{\mu\nu} = (+, -, -, -)$ is the Minkowski metric and $\mathbb{I}_4$ is the 4×4 identity matrix. In this notation the Dirac equation can be expressed as

$$\hbar(i\gamma^\mu\partial_\mu - \frac{mc}{\hbar})\psi = 0. \tag{B.3}$$

The fifth Gamma matrix is defined as

$$\gamma^5 = i\gamma^0\gamma^1\gamma^2\gamma^3 = \begin{pmatrix} -\mathbb{I} & 0 \\ 0 & \mathbb{I} \end{pmatrix}. \tag{B.4}$$

In Dirac representation, γ^k remains the same, but γ^0 is different, accordingly γ^5 is also different,

$$\gamma^0 = \begin{pmatrix} \mathbb{I} & 0 \\ 0 & -\mathbb{I} \end{pmatrix} \quad \text{and} \quad \gamma^5 = \begin{pmatrix} 0 & \mathbb{I} \\ \mathbb{I} & 0 \end{pmatrix}. \tag{B.5}$$

In Sakurai's notation, the definition of the fifth matrix is slightly different, i.e. $\gamma_5 = \gamma_1\gamma_2\gamma_3\gamma_0$. The fifth matrix (B.4) satisfies

$$(\gamma^5)^2 = \mathbb{I}_4, \quad (\gamma^5)^\dagger = \gamma^5, \quad \text{and} \quad \{\gamma^5, \gamma^\mu\} = 0, \quad \mu = 0, 1, 2, 3. \tag{B.6}$$

With the definition of the Gamma matrices, the left-handed and the right-handed projection operators are defined as

$$P_L = \frac{1}{2}\left(1 - \gamma^5\right) \quad \text{and} \quad P_R = \frac{1}{2}\left(1 + \gamma^5\right). \tag{B.7}$$

Therefore, the chiral projections are

$$\psi_L = \frac{1}{2}\left(1 - \gamma^5\right)\psi = \begin{pmatrix} \mathbb{I} & 0 \\ 0 & 0 \end{pmatrix}\psi \quad \text{and} \quad \psi_R = \frac{1}{2}\left(1 + \gamma^5\right)\psi = \begin{pmatrix} 0 & 0 \\ 0 & \mathbb{I} \end{pmatrix}\psi \tag{B.8}$$

where $\psi = \begin{pmatrix} \psi_L \\ \psi_R \end{pmatrix}$. ψ_L and ψ_R are left-handed and right-handed two component Weyl spinors, respectively. As we stated in the last subsection, chirality and helicity coincide for massless Dirac fermions. In the limit of zero mass, Dirac equation (B.3) reads

$$\hbar \begin{pmatrix} 0 & \sigma^\mu k_\mu \\ -\sigma^\mu k_\mu & 0 \end{pmatrix} \begin{pmatrix} \psi_1 \\ \psi_2 \end{pmatrix} = i\hbar\gamma^0\partial_0 \begin{pmatrix} \psi_1 \\ \psi_2 \end{pmatrix}, \quad \mu = 1, 2, 3. \tag{B.9}$$

If one take $\psi_1 = \psi_L$ and $\psi_2 = \psi_R$, then the last equation separates into two equations:

$$\begin{aligned} c\hbar\sigma^\mu k_\mu \psi_R &= i\hbar\partial_t\psi_R \\ c\hbar\sigma^\mu k_\mu \psi_L &= -i\hbar\partial_t\psi_L. \end{aligned} \tag{B.10}$$

APPENDIX C: TABLES

Table C.1. Fitted transfer integrals (eV) at ambient pressure (ap) and with uniaxial strain of 2 kbar along the a-axis (a2) and 3 kbar along the b-axis (b3) at room temperature (RT) and 8K. The table is created by using the data previously presented in Reference [9].

	T = RT				T = 8K		
	ap	a2	b3	tb	ap	a2	b3
c1	-0.0476	-0.0358	-0.0393	-0.049	-0.0511	-0.0461	-0.0405
c2	0.0093	0.0029	0.0287	0.0018	0.0323	0.0373	0.0397
c3	-0.0101	-0.0173	-0.0195	-0.03	-0.0267	-0.0245	-0.0267
p1	0.1109	0.1154	0.1176	0.142	0.1296	0.1220	0.1251
p2	0.1081	0.1075	0.1226	0.123	0.1241	0.1276	0.1336
p3	0.0151	0.0085	0.0156	0.023	0.0152	0.0133	0.0190
p4	0.0551	0.0559	0.0537	0.062	0.0513	0.0507	0.0515

Table C.2. The transfer energies t_x and the coefficients K_x are given using the data at $P_a = 0$ and at $P_a = 2$ kbar. The table is created by using the data previously presented in Reference [5].

x	c1	c2	c3	p1	p2	p3	p4
K_x(eV kbar^{-1})	0.167	-0.025	0.089	0.011	0	0	0.032
t_x(eV)	0.048	-0.020	-0.028	0.140	0.123	-0.025	-0.062